TECHNISCHE UNIVERSITÄT WIEN

isas

Masterarbeit

Characterization of narrowband MEMS based detectors for integrated mid-infrared gas sensing

ausgeführt zum Zwecke der Erlangung des akademischen Grades eines Master of Science bzw. Diplom-Ingenieurs, eingereicht am

Institut für Sensor- und Aktuatorsysteme
Technische Universität Wien

vorgelegt von:
Lukas Rauter
A-9232 Rosegg

betreut von:
Univ. Prof. Dipl.-Ing. Dr.techn. Franz Keplinger
Dr. Thomas Söllradl
Dr. Cristina Consani

Wien, am 30. November 2018

Eidesstattliche Erklärung

Ich erkläre an Eides statt, dass ich die vorliegende Masterarbeit selbstständig und ohne fremde Hilfe verfasst, andere als die angegebenen Quellen und Hilfsmittel nicht benutzt bzw. die wörtlich oder sinngemäß entnommenen Stellen als solche kenntlich gemacht habe.

Wien, am 30. November 2018

Unterschrift (Lukas Rauter)

Inhaltsverzeichnis

Abstract

The underlying project of this work is performed in cooperation with Infineon Technologies Austria AG and the Johannes Kepler University of Linz. Work is done on the development, characterization and optimization of an optical carbon dioxide sensor, based on mid infrared absorption by the gaseous CO_2 molecules. The construction of such a sensing system requires the integration of a mid-IR sensitive detector, attached to a waveguide, a radiation source and a wavelength selective filter structure. In this master thesis the experimental characterization of three different detectors will be presented. In addition to a simple bolometer and a P-N diode, a newer concept, a so-called vertical cavity enhanced detector is examined more closely. A big advantage of this detector is that it has an directly integrated wavelength selective filter, in the form of a Bragg mirror, tailored for 4.26 microns, according to the absorption spectrum of CO_2.
At the end it is demonstrated that the vertical cavity enhanced detector outperforms the other two and the cavity induces an increase in responsivity by a factor 7.1. As such this design can be easily optimized and integrated to specifically enhance the detector response around the design wavelength.

Keywords: sensor; detector; photonic crystal; mid-IR; Bragg mirror;

Acknowledgement

First and foremost I would like to thank Prof. Dr. Franz Keplinger, my main supervisor, Dr. Cristina Consani and Dr. Thomas Söllradl. Only through them I got the possibility to write my master thesis by an engagement at the CTR AG. Through extensive discussions and the professional competence of my supervisors, I was always well accompanied and advised. I would also like to thank all the other employees of CTR AG for their support and my inclusion into the team. The good cooperation has contributed significantly to the success of this work and I will always like to remember my time as a graduand at CTR AG. I would also like to thank my sister, my parents, relatives and friends for their support throughout the entire period of study and the encouraging words in troubling times.

Mein Dank gilt in erster Linie Herrn Prof. Dr. Franz Keplinger, meinem Hauptbetreuer, Frau Dr. Cristina Consani und Herrn Dr. Thomas Söllradl. Erst durch sie wurde mir diese Diplomarbeit durch eine Anstellung bei der CTR AG ermöglicht und durch ausführliche Diskussionen und ihre fachliche Kompetenz stets gut begleitet. Auch allen anderen Mitarbeitern der CTR AG möchte ich herzlich für ihre Unterstützung und meine Aufnahme ins Team danken. Die gute Zusammenarbeit hat maßgeblich zum Gelingen dieser Arbeit beigetragen und ich werde mich immer wieder gerne an meine Zeit als Diplomand in der CTR AG erinnern.
Danken möchte ich außerdem meiner Schwester, meinen Eltern, Verwandten und Freunden für ihre Unterstützung während der gesamten Studienzeit und für die aufmunternden Worte in manch nervenzerrenden Zeiten.

Chapter 1.

Introduction

1.1. Motivation

Over the last few years, society has been increasingly concerned with climate change, inter alia caused by greenhouse effect. This and other factors, such as air quality monitoring and safety regulations lead to large interest in trace gas monitoring. Additionally, modern medical, industrial and military applications pushed further technical development of gas sensor devices to much higher levels. The main efforts are to shrink the size of such sensor systems down to the micro and nano scale, so they can be fully integrated into small technical components and even portable units. Furthermore they should show a high sensitivity, be cheap in fabrication and robust relating to mechanical and thermal stress. In this context MEMS based sensors are of particular interest, due to the integrability and low fabrication costs. The Carinthian Tech Research AG, in cooperation with Infineon Technologies Austria and the Johannes Kepler University of Linz, are working on a project about the design, fabrication and characterization of a fully integrated CMOS compatible sensor system for carbon dioxide (CO_2) detection. CO_2 and several other gases show specific absorption peaks within the mid-infrared region. This motivated the choice of a sensing scheme, based on optical absorption of radiation. The development of miniaturized, sensitive detectors for mid-infrared radiation, which are a key component of optical sensors, is challenging. This thesis focuses on the experimental characterization of mid infrared detectors previously developed within this project.

1.2. State of the art

One distinguishes between two major types of gas sensors depending whether the composition or concentration of certain gases or mixtures of gases should be measured. If the gas type is already known and the concentration of it should be detected within any mixture of gases, e. g. the concentration of CO_2 in air, the method is called quantitative gas analysis.
Such sensing systems are based on different principles. One fundamentally differentiates between two main technologies: Chemical sensors and physical sensors.

1.2.1. Chemical gas sensors

Chemical gas sensors are based on conversion of chemical information into electrical signals. For this, the sensor must have a reactive unit, which is able to interact with the substance to be measured. A simple example is the zinc oxide gas sensor, which reduces its resistance at high temperatures as the concentration of carbon monoxide increases, due to accumulation of gas molecules on the reactive surface of the sensor.
At the current state of research, metal oxide semiconductor sensors are of high interest and already fabricated for sale by some companies.

Metal oxide semiconductor (MOX) sensors MOX based sensing systems work by changes of conductivity within the metal oxide induced by adsorption or desorption of a gas. The effect was discovered and first demonstrated in 1962 on zinc oxide thin film layers. [1] Basically those chemosensors are consisting of a sensitive semiconductive layer on a ceramic substrate. Through adsorption of gaseous molecules and subsequent chemical reactions on the sensor surface, changes of conductivity appear due to changes in the electron density. Depending on whether oxidizing or reducing compounds interact, the number of electrons within the sensitive layer is decreasing or increasing. This can be measured as a change of current using electrodes integrated between the semiconductor and the ceramic base. To remove the gas molecules bound to the surface and regenerate the sensor, the system has to be heated. This can for example be done by platinum meanders set under the substrate. A schematic of a MOX sensing structure is shown in figure 1.1. [2]
Most common sensitive layer materials are e.g. tin(IV) oxide, tungsten(VI) oxide or gallium(III) oxide with operating temperatures of about 100 to 600°C. Such devices are sensitive for several gas types. To increase responsivity and selectivity for certain gases, precious metal catalysts have to be deposited onto the sensor surface.

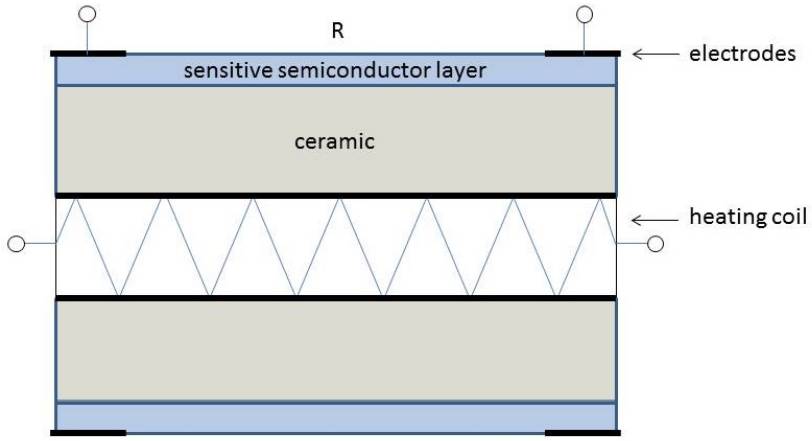

Figure 1.1.: Schematic of MOX sensor structure (in style of [3]).

1.2.2. Physical gas sensors

Physical sensors are devices that convert a measured physical information into an electrical signal. The measured variable can be mechanical, magnetic, thermal or radiation-based. Physical gas sensors work exclusively thermally or by use of electromagnetic radiation. The most important concepts at the current state of research are based on optical or photoacoustic effects.

Optical sensors Optical gas sensors are electronic devices that belong to the subarea of optoelectronics. Modern miniaturized concepts are summarized as integrated optics. Techniques like epitaxy, lithography and doping got adopted from microelectronics and are now offering the necessary conditions for integrated optics fabrication. Basically they use three different methods to detect substances. These are atomic absorption spectrometry, optical emission spectrometry and atomic fluorescence spectrometry.
The most commonly used and simplest method is non-dispersive infrared (NDIR) and based on absorption spectroscopy by the gas to be measured. NDIR provides fast responses und high gas specificity without detecting other gases than desired. The principle is based on the fact that trace gases show specific absorption peaks within the mid-IR region of the electromagnetic spectrum (Figure 1.2). A sensing system, operating on this method, usually consists of an infrared source, a cell containing the gas sample, a reference non-absorptive

region in order to be able to determine the gas concentration by comparison of the radiation intensity, and a detector. The radiation source emits in direction of the sample cell, where intensity is lost by absorption from the target gas.The light intensity is read out by the detector. The intensity is measured in presence and in absence of the target gas (either within the same sample cell or by using a different reference cell, typically filled with an inert gas). Comparison between such measured intensities allows to determine the transmittance through the gas sample and therefore its concentration by using the Beer-Lambert law, as explained below.

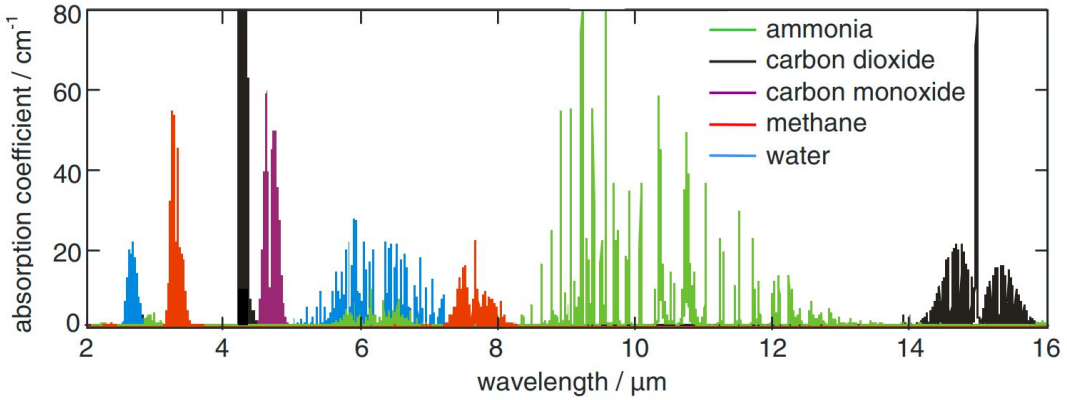

Figure 1.2.: Section of atmospheric absorptionspectrum; in region 4.24 µm - 4.28 µm the absorption peaks of CO_2 are clear visible. [4]

When using broadband light sources, a wavelength selective filter is required within the sensing system in order to be selective to the desired substance. Carbon Dioxide, which is our gas of interest, has its absorption band centered at 4.26 microns. Thus, the maximum of the radiation spectrum of the sensor should be at this position, with an as narrow as possible FWHM, in order to avoid the influence of other gases. Physically such an NDIR sensor can be described according to Beer-Lamberts law:

$$I(t) = I_0(t) \cdot \exp\left(-\alpha_\lambda L C\right), \tag{1.1}$$

where $I(t)$ is the output light intensity, I_0 is the input light intensity, α_λ is the absorption coefficient at the measurement wavelength, L is the optical path length of the interactive region and C is the concentration of the gas sample. [5]
Within the interaction zone, interaction between photons of the infrared electromagnetic radiation and the molecules of the measuring gas occurs. Molecules are not rigid structures,

but constantly in motion, with bond lengths and angles fluctuating around average values. The molecule can be described as a quantum mechanical harmonic oscillator. For this one obtains a potential curve with discrete energy levels for vibrations of different energies. The energy difference ΔE between the allowed levels is equidistant $h\nu_{\text{vib}}$ (Figure 1.3). Each vibration level has an associated quantum number v, which can be used to calculate the energy of the respective level:

$$E = h\nu_{\text{vib}}(v + 1/2) \tag{1.2}$$

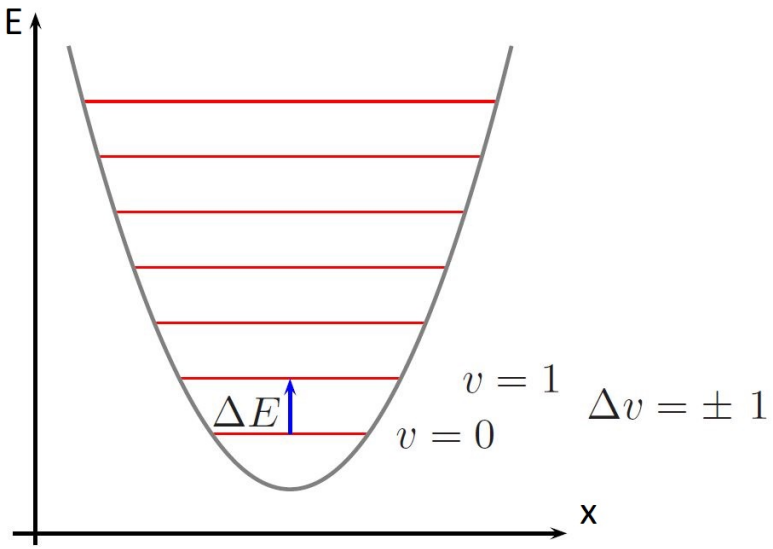

Figure 1.3.: Potential curve for quantum mechanical harmonic oscillator. [6]

Considering the composition of the inner energy of a molecule, which consists of electrical, vibrational and rotational energy, one can say: Within the region of ultraviolet radiation mostly electronic transitions are excited, while in the infrared vibrational and rotational transitions are excited. Furthermore it hast to be observed that the infrared spectrum of a gaseous substance differs significantly from that of a liquid or solid. The absorption bands of the gas spectrum split into discrete sharp lines (Figure 1.4).
This happens because vibrational transitions couple to rotational transitions, which usually have smaller energy spacing. In the liquid state, these lines are broadened by collisions of the particles with each other. Like vibrational energy, also the rotational energy is quantized. For a molecule that absorbs infrared radiation of energy $\Delta E = h\nu$, where h is the Planck's constant and ν the light frequency, the system can be transferred to an excited state in compliance with two selection rules for permitted state changes of the total energy. For the

vibrational quantum number v and the rotational quantum number J applies: $\Delta v = \pm 1$ and $\Delta J = \pm 1$. At room temperature most of the molecules are in vibrational ground state $v = 0$ and radiation absorption usually leads to $v = 1$. The rotation quantum number must either increase or decrease by 1, as zero transitions are forbidden due to the selection rules. [6] Carbon dioxide has a high absorption coefficient for light in the region 4.2 - 4.3 µm (Figure 1.2). This allows very short optical path lengths of the interaction zone and further miniaturization of the whole sensing system, while still having good detection limits.

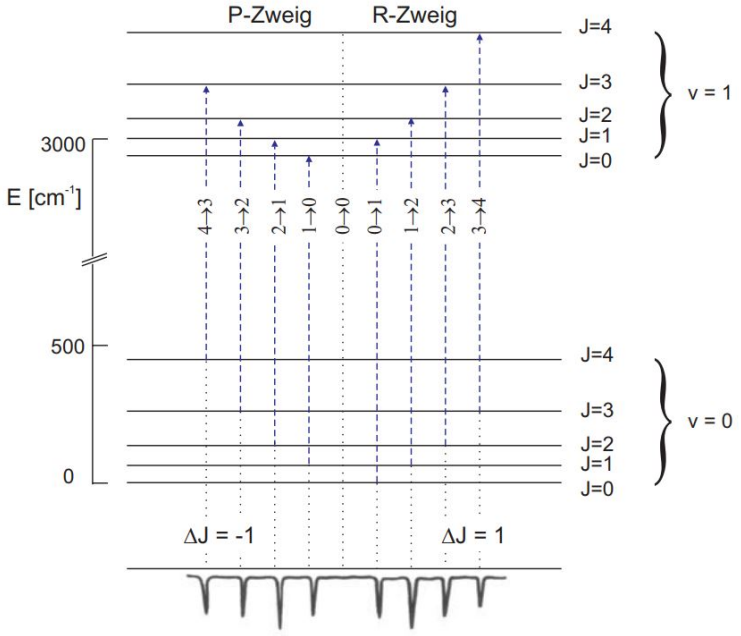

Figure 1.4.: Rotation transitions between the vibration levels for $v = 0$ and $v = 1$ and the resulting rotational vibration spectrum. [6]

Photoacoustic sensors Photoacoustic sensors are based on the photoacoustic effect, which describes the generation of acoustic waves by radiation absorption in gaseous, condensed or solid phases. If light of a certain wavelength gets absorbed by a sample, the molecules are excited to a higher rotational, vibrational or electronic level, analogous to the optical gas sensors. Afterwards, the energy is again released either in form of electromagnetical radiation or kinetic energy through collisions with adjacent atoms or molecules. Because of a much faster relaxation by collisions than by spontaneous emission, almost the whole energy gets converted to kinetic energy. This leads to a local increase of temperature and therefore of pressure, which is described by the kinetic theory of gases. If the intensity of the incident light is now changing periodically, what can be easily achieved by modulated

laser irradiation, pressure changes appear. Under appropriate circumstances those can be detected as acoustic waves [7]. The generated pressure waves move to the membrane of a sensitive microphone. The amplitude of the detected acoustic waves is then proportional to the concentration of measured molecules (Figure 1.5). [8]
Photoacoustic sensors require a minimal sample preparation and the technique is suitable for opaque materials. A disadvantage of this sensor method is that it is not completely capable of being integrated due to the gas volume, which is necessary to detect pressure oscillations of the gas sample. [9]

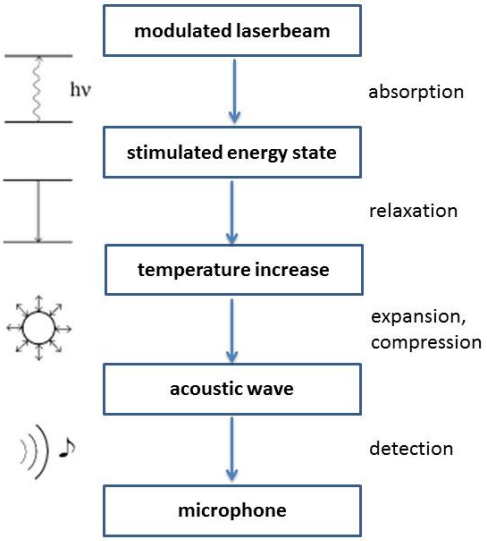

Figure 1.5.: Schematic of photoacoustic effect (in style of [10]).

Chapter 2.

Concept for an integrated optical gas sensor

In this chapter, the sensor concept, developed within the scope of the project, and various possibilities for realization of the individual components are presented.

2.1. Integrated CO_2 gas sensor based on evanescent field absorption

Due to requirements of integrability and selectivity the CO_2 sensor, developed and characterized in this project, is based on NDIR optical sensing. This method has the advantages that a primary effect (i.e. absorption) is measured rendering them faster compared to photoacoustic devices and they are selective, different from MOX sensors, which react to several gases. As previously mentioned (Section 1.2.2), such a sensor consists of four fundamental components, an emitter, a waveguide, a filter structure working as wavelength selective element and at last a detector (Figure 2.1).

The working principle slightly differs depending on which components are used. For an integrated design, an emitter radiates light on a grating, through which it is coupled into a waveguide. Through the waveguide, the light is propagating towards the detector, while simultaneously interacting with the surrounding gas molecules by evanescent field absorption, explained later. In a final step the remaining radiation intensity impinges on a detector and gets usually analyzed by reading out changes of resistance. Somewhere within this system there must also be the wavelength selective filter, which ensures that only radiation in range of the desired wavelength (corresponding to the CO_2 absorption

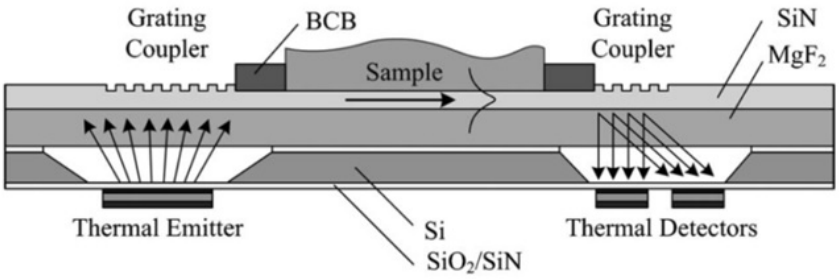

Figure 2.1.: Schematic of sensing concept. [11]

peak at 4.26 µm) strikes the detector.
For all of those construction units it is possible to use different types to optimize the sensing system regarding responsivity, sensitivity, durability and fabrication costs.

2.1.1. Mid-IR radiation sources (Emitters)

Thermal emitter The most commonly applied sources for mid IR radiation are filaments of SiC or doped polycrystalline Si, which emit, when heated, isotropic, incoherent, broadband electromagnetic radiation, almost like a black body radiator. A black body is an idealized physical body that absorbs all incident electromagnetic radiation and complies the equation $\alpha = \epsilon = 1$ (α absorption coefficient, ϵ emission coefficient). Thermal radiation is generated when charge carriers in matter are excited to higher energy states during the heating process. This energy difference can be transferred by collisions to adjacent particles or the stimulated electrons get back in ground state by spontaneous emission of electromagnetic radiation. The spectral distribution of the emitted light is described by Planck's law of thermal radiation and only depends on the radiators temperature, while the total emitted radiant power can be determined by Stefan-Boltzmann law. [12]

$$P = \epsilon \cdot \sigma \cdot A \cdot T^4 \tag{2.1}$$

with:
ϵ ...emissivity
σ ...Stefan-Boltzmann constant
A ...radiating area

The continous spectrum has all wavelengths from zero to infinity with a peak at a certain

wavelength. According to Wien's law the peak shifts to shorter wavelengths as the temperature of the black body increases. [13] For sensing usually only a specific band within the electromagnetic spectra is required. To get a narrowband and directional emission of mid IR radiation, a filter structure has to be included, e.g. a dielectric multilayer stack, working as a Bragg mirror.

Mid-IR light emitting diodes (LEDs) Light emitting diodes are photonic devices available for different wavelengths, what is mainly depending on the base semiconductor material and the doping. Basically, LEDs are working like semiconductor diodes which are generating light in forward direction. An n-doped semiconductor forms the base of the diode structure with a thin p-doped layer on top (Figure 2.2). If one applies voltage, a

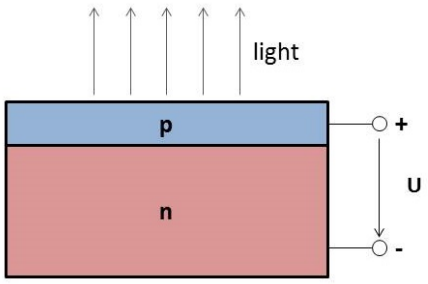

Figure 2.2.: Schematic LED operating principle (in style of [14]).

charge carrier avalanche is growing at the p-n junction. After transfer of an electron from the n- to the p-layer, this then passes into the energetic lower valence band. This transition is called recombination and can be interpreted as the coincidence of an electron from the conduction band and a hole in the valence band. The energy released during recombination is usually emitted as radiation within a direct semiconductor. Due to very small extension of the p-doped layer in one dimension, the light is able to escape from the structure and even at very low currents radiation emission is perceptible. [14]
Difficulties of integrating LEDs on a Si platform, because of their special semiconductor materials (usually GaSb or InGaAs heterostructures) could be overcome by cointegration with e.g. InAs. Growing these structures by liquid phase epitaxy processes makes them a very cost-effective alternative for use as radiation source in gas sensors. [15]
Nevertheless, the typical emitted powers in the mid-IR are low, compared to emitters in the visible or near infrared, and typical bandwidths are broad, such that a spectral filter is still necessary for most applications.

Quantum cascade lasers Quantum cascade lasers (QCLs), which were first developed in 1994 by J. Faist et al. at Bell Laboratories, attracted attention as new light sources for gas sensing devices due to their versatility and performance within the mid IR regime. Typical characteristics of QCLs make them offer various advantages compared to other infrared emitters, e.g. their emission up to watts of output power and their narrow emission bandwidth, leading to an enhancement of responsivity and sensitivity. [16]
In contrast to conventional interband diode emitters, quantum cascade lasers do not emit light because of recombination of electrons from the conduction band with holes from the valence band. Emission of radiation is happening due to transitions of electrons between quantized sub bands of quantum wells (QWs) within the conduction band. QWs are potential wells with only discrete energy values which can be fabricated by molecular beam epitaxy. This growth technique works by reaction between thermally generated molecular beams and the surface of a cristalline subrate. Charge carriers are tunneling from ground state of one QW to an energetically lower state of an adjacent QW, when an electric field is applied. The structure is consisting of two main sections: the active region and the injector. The active area constitutes an energetic three-level system where the laser transition is actually taking place, when charge carriers migrate from e.g. level three to level two. For necessary population inversion in this case the lifetime of energy level 3 has to be much higher than for lower level 2. Further, the charge carriers get to the injector from where they get injected again to level 3. Two adjacent active regions are always seperated by an injector. The wavelength of emitted radiation depends on the thickness of the quantum wells and barrier layers of active region (Figure 2.3). For single frequency operation it is necessary to add a Bragg grating. Main disadvantages of QCL, compared to the other concepts are their limited integrability due to compatibility of exotic materials with classic Si-based photonics and the high costs. A possible material combination for realization of a QCL is GaInAs for quantum wells, which are seperated by AlInAs barriers, deposited onto an InP substrate. [17]

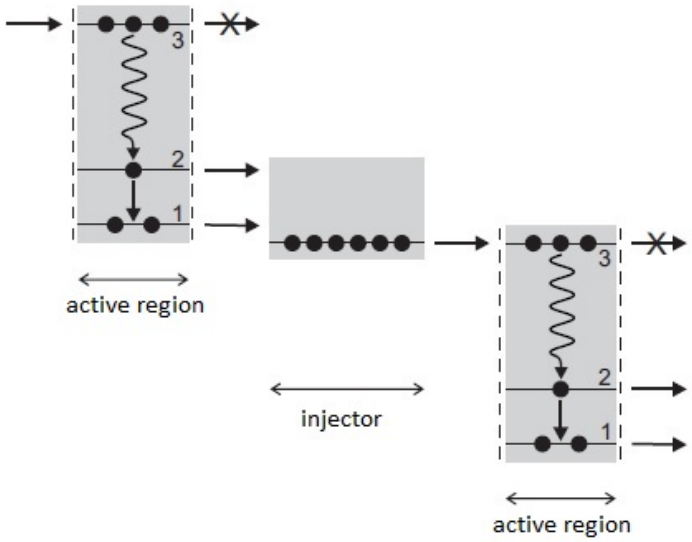

Figure 2.3.: Schematic of QCL funcion principle. [17]

Vertical-Cavity Enhanced Resonant Thermal Emitter (VERTE) In 2005 I. Celanovic et al. proposed the VERTE, which is a simple alternative for integrated photonic based sensors designed to enhance sensing performance and efficiency. Further a similar structure was designed and tuned to the CO_2 absorption region by Gerald Pühringer from Johannes Kepler Universtiy Linz and the team from CTR AG Villach, and later characterized. The VERTE consists of a resonant cavity sandwiched between a silver mirror and a Bragg mirror of alternating silicon and silicon dioxide layers, tailored for enhancement of a specific wavelength, deposited onto a Si substrate. The silver layer acts as a cavity mirror as well as a thermal radiation source (Figure 2.4).
The multilayer stack of alternating quarter-wave layers of Si and SiO_2 creates a narrowband electromagnetic radiation enhancement in the cavity layer and further leads to selective thermal radiation. Absorption measurements showed a four times enhancement of emission at the design wavelength compared to bare metal. [18]

2.1.2. Waveguides and evanescent field

Waveguides are essential structures for light propagation providing minimal loss of energy. Usually, they are used as connection between emitter and detector in sensing devices. Like optical fibres, dielectric waveguides can be directly involved in sensing and even work

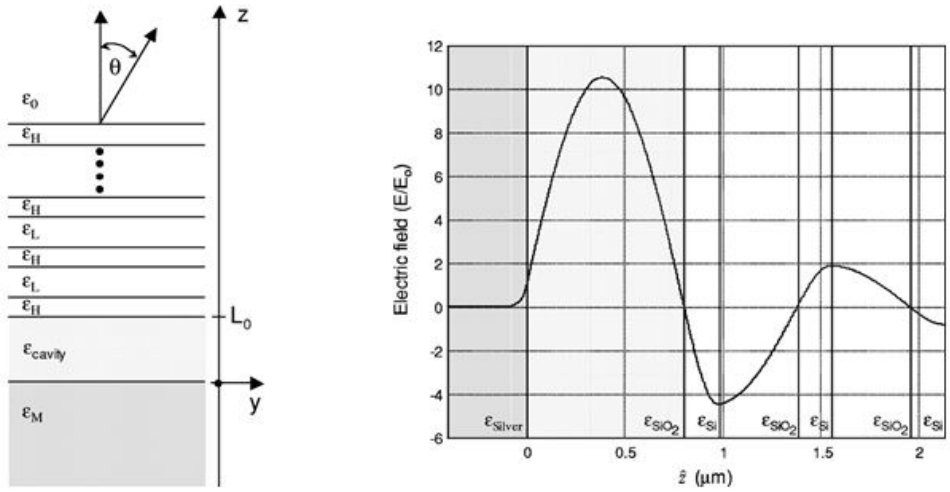

Figure 2.4.: Schematic of cross-section of VERTE structure and simulation of maximum field enhancement within the cavity. [19]

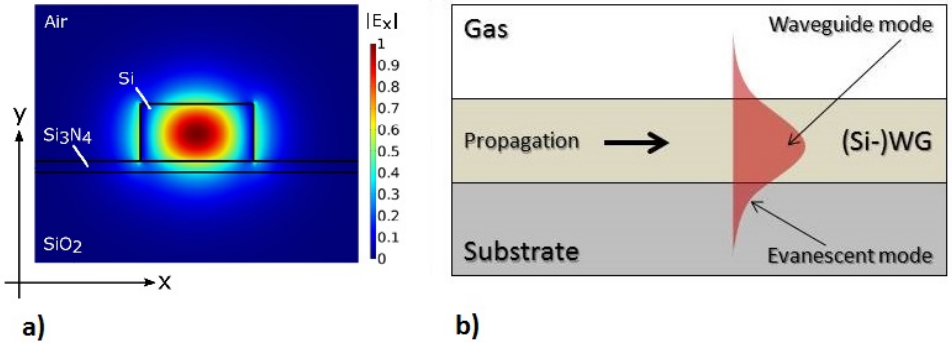

Figure 2.5.: (a) Cross-sectional simulation of evanescent field and (b) schematic of exponential decay (in style of [21]).

as sensing element itself. This is possible due to the phenomenon of evancescent field absorption, where a small fraction of the electromagnetic field is extending outside the waveguide and therefore is able to interact with the surrounding CO_2 molecules. The evanescent field decays exponentially with the distance from the waveguide. Due to the evanescent tail of the field, the total radiation intensity, propagating through the waveguide can decrease by absorption from the cladding materials. [20]

Especially silicon waveguides with subwavelength cross sections are efficient for use as sensing units in gas sensing devices due to certain properties of Si. First of all, it is transparent for electromagnetic radiation within the mid IR regime between 3 and 8 µm. The large contrast of refractive index between Si and typical cladding materials, e. g. SiO_2, allows a very strong guidance and allows to achieve small curvature radii for bent waveguides.

Beside more advantages compared to other semiconductor materials, like e.g. the good thermal conductivity and its robustness, Si-based integrated optical systems provide low manufacture costs at high integration density. [22]
By forming structures like spirals or meanders it is possible to extend interaction time and length on a very small area, causing enhancement of sensitivity. [23]

2.1.3. Mid-IR detectors

Infrared detectors can be devided into two classes: Thermal and photon IR detectors.

Thermal detectors According to their working principle IR thermal detectors are classified into three main groups: thermoelectric, pyroelectric and bolometer IR detectors. All of them are working on absorption of infrared radiation, which gets converted into thermal energy. Sensitive components show an increase of temperature, what induces a change of certain quantities like e.g. resistivity.

- Thermopile
  Thermopiles consist of several thermocouples connected in series, resulting in the addition of individual small thermoelectric voltage signals and consequently in enhancement of responsivity. Thermocouples are applicable within a broad temperature range from around minus 200 °C up to 3000 °C. The function principle of those sensors is based on Seebeck effect. Therefore two contacts of different metals of an opened conductive circuit have to be set on different temperatures T_1 and T_2. Due to temperature difference $\Delta T = T_2 - T_1$ between the two contacts the thermoelectric field E occurs and generates a thermoelectric current, if the endings are connected (Figure 2.6). So thermal energy gets directly converted to electrical energy. For most metal combinations E is in scale of some micro- or millivolts. For sufficient small temperature differences E can be calculated as [24]

$$E = a\Delta T + b\Delta T^2 \tag{2.2}$$

  where a and b are thermoelectric matter constants of the two metals. By composition of several thermocouples, a thermopile detector is formed, where wires of the same

metal are always parallel to each other in a row. Then one row is the active layer, which is hit by radiation and heated up, the other one is the reference layer at a certain reference temperature.

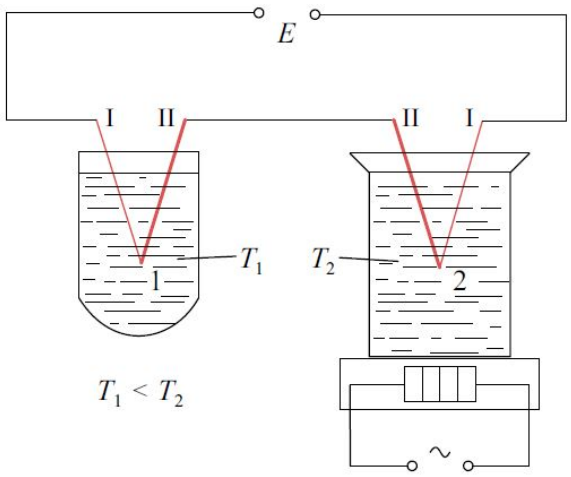

Figure 2.6.: Measurement principle of a thermocouple with two different metals I and II. At one end the different metal wires are connected, where a thermoelectric voltage is generated. Between the two non connected wire endings then a voltage is measurable, according to Seebeck effect. [24]

- Bolometer

  The main component of a bolometer detector is a thermally isolated resistive element made of a material with a large temperature coefficient α

$$\alpha = \frac{1}{R} \cdot \frac{\mathrm{dR}}{\mathrm{dT}} \tag{2.3}$$

  with

  R ...resistance and T ...temperature

  The measurement principle is based on the change of resistivity of the detector material as a result of the heating process induced by incident radiation (Figure 2.7).

  To run the detector a constant current I has to be applied. Further the voltage difference ΔV can be measured and ΔT calculated. [25]

$$\Delta V = IR\alpha\Delta T \tag{2.4}$$

Depending on whether the detector material is metallic (positive temperature coeffient) or a semiconductor (negative temperature coefficient) the detector is termed resistance temperature detector or thermistor (thermally sensitive resistor). Metals used usually like gold or nickel, show a temperature coefficient in range $0.3 - 0.6\%/°\mathbf{C}$. Actually thermistors are much more effective due to temperature coefficients around $4\%/°\mathbf{C}$.

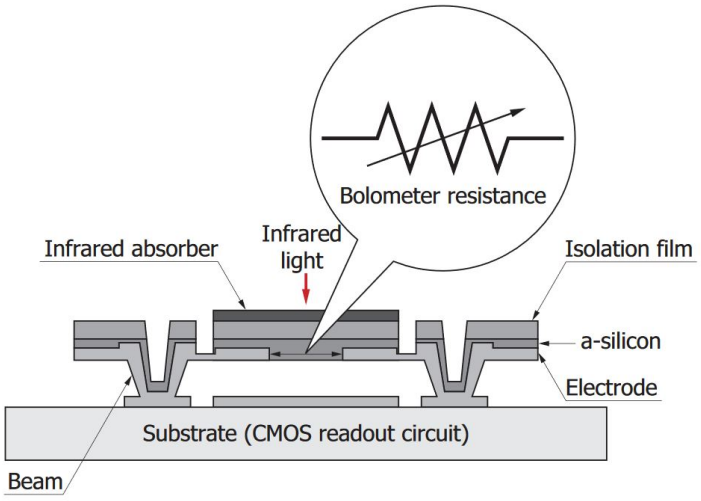

Figure 2.7.: Schematic representation of a bolometer principle used for infrared radiation detection. [26]

- Pyroelectric detectors
  Pyroelectric detector devices are based on temperature sensitive pyroelectric semiconductor crystals, which have a temperature dependent internal dipole moment (Figure 2.8). Basically, the crystals are consisting of polar single unit cells with each of them having a dipole moment. The macroscopic field generated by the dipole moment is compensated by charge carriers (e.g. free electrons or ions) of the surrounding area, which get absorbed by the crystal surface, and thus the field is shielded to the outside. If the material temperature is constant, dipole moment does not change. If it is heated up, for example by incident electromagnetic radiation, the spontaneous polarization, what is the dipole moment by unit volume, decreases. This leads to short-term shifts of surface charges or to an electrical voltage, until a charge balance has set again. If one now applies conductive electrodes to the outer surfaces of the crystal and connects them with an ammeter with low internal resistance, a current

flow is measurable. This charge transport, called pyroelectric current, is generated by the endeavor of the free charge carriers to rebalance the shifted polarization. Of course, a completely analogous effect occurs during cooling. The main disadvantage of pyroelectric sensors is the measurability of only modulated signals. [27]

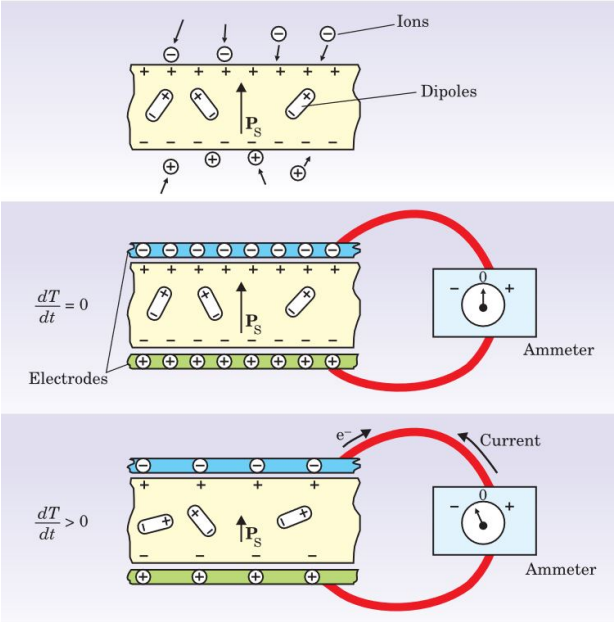

Figure 2.8.: Behavior of pyroelectric crystal due to temperature change. Pyroelectric current is measurable by conductive electrodes. [27]

Photodetectors Photon detection concepts are based on different phenomena induced by incident photons interacting with electrons in matter, causing changes of electronic state, usually in semiconductor material. Advantages of photon IR detectors, compared to thermal concepts, are better responsivity and lower noise levels. The main three effects, which are usually applied for infrared detection, are: Photoconductivity, photovoltaic and photoemissive effect.

- Photoconductivity detectors
  The simplest concept of a photodetector makes use of increasing electrical conductivity or decreasing resistivity, due to photoionization of impurities in crystal structure or interband transitions. One distinguishes between the intrinsic and extrinsic effect.
  The intrinsic effect runs as follows: If an incident photon has energy larger than the bandgap of the semiconductor, a transition of electrons to the conduction band

is possible. Most materials used for photodetection devices, e.g. Si and Ge, have bandgaps between 0.4 eV and 2.4 eV at room temperature, restricting the principle to detection of visible or near IR light. To specify the detector material for radiation within the mid IR range, materials such as PbS, PbSe and PbTe are used.
The extrinsic form of photoconductivity requires photons of lower energy compared to those for intrinsic photoconductivity, to excite electrons from impurities into the conduction band or from the valence band to impurities. [25]
Another possible impact of incident radiation can result in higher mobility of charge carriers by increasing kinetic energy through optical excitation.
It should be considered that photoconductive detectors have a temperature dependent bulk resistance. If the resistance changes due to temperature fluctuations, a signal is generated, which can often not be distinguished from the photoconductive signal. The simplest solution to this problem is to keep the detector temperature constant by use of certain cooling technologies. [28]

- Photovoltaic detectors
  The simplest version of a photovoltaic-based detector is a PN-diode (Figure 2.9). Within the barrier layer (depletion zone) of a semiconductive p-n junction, a boundary between two different semiconductor materials inside a single semiconductor crystal, p-type and n-type (p contains an excess of holes, n contains an excess of electrons), almost no free charge carriers exist. This is a result of carrier diffusion. The electric field within the barrier layer prevents a current flow in an external circuit, except for slight leakage currents.
  By illumination of the p-n junction, electron-hole pairs are generated by optical excitation and further get seperated by the internal electrical field. Due to drifting of charge carriers towards the p- and n-doped sectors, a resulting current is measurable, which is proportional to the power of incident light.
  The separation of electrons and holes within the depletion zone stops working properly, at very high irradiation intensities because of an increase in the recombination of charge carriers. In order to prevent such perturbation it is necessary to apply a reversed bias voltage, which is then added to the diffusion voltage and supports the charge separation. [29]

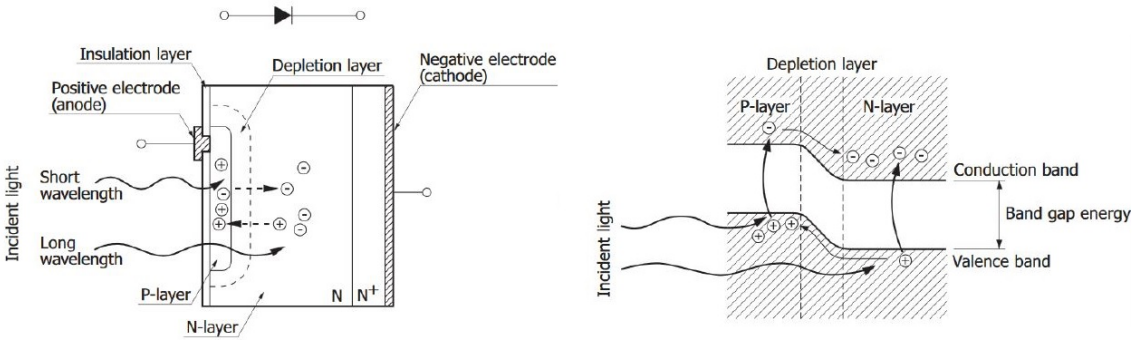

Figure 2.9.: Operating principle of a PN-diode detector: charge carriers (electrons) get lifted over the valence-conduction bandgap and further accelerated by the electrical field. [30]

- Photoemissive effect

  The photoemissive effect occurs, when photons impact on a metal or semiconductive material surface (photocathode). If the transferred photon energy is at least as high as the binding energy of an electron, the electron can be emitted and further collected by an anode. Whether the photocathode is a metal or a semiconductor, depends on the radiation which should be detected. The binding energies of electrons in metal are in range of some electron volts, so only visible or ultraviolet light can be measured. In semiconductor materials an incident photon mostly excites an electron from the valence band into the conduction band. To cause photoemission in semiconductors the minimum energy required is that which will excite an electron to an energy level higher than the potential barrier at the surface, which is still less than for metallic photocathodes. This allows detecting radiation up to very near infrared, but is still not a working option for detecting within the mid-IR. [25]

2.2. Silicon based detector concepts for an integrated CO_2 gas sensor

In this chapter, the three detectors investigated and characterized during this thesis are described. The main focus is on the vertical cavity enhanced detector.

2.2.1. Doped polysilicon wire

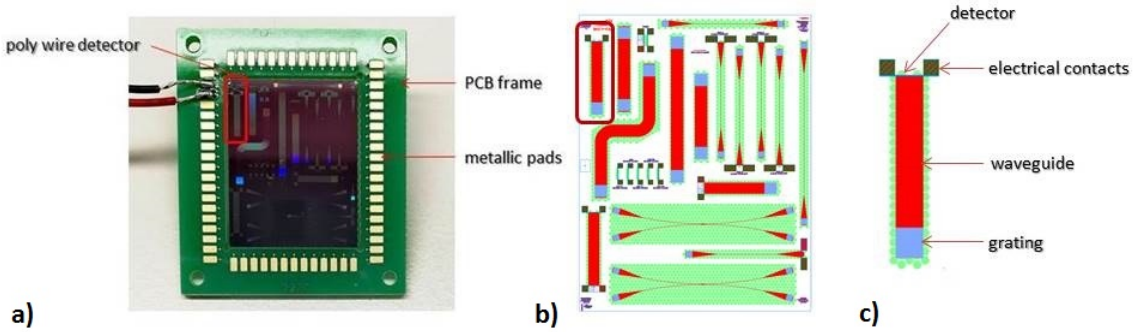

Figure 2.10.: a) Chip with a doped polysilicon wire detector structure, bonded with PCB frame. b) Layout image of chip with poly wire in left upper corner. c) Poly wire detector structure.

The doped polysilicon wire detector is working on the principle of a bolometer (see section 2.1.3). It is a thermal detector where a change in temperature induces a change in resistance, which can be read out by electrical contacts. The future idea for reading out the signal is to integrate the wire into a quarter Wheatstone bridge as variable resistance.
In practice, the structure is a phosphor-doped polysilicon layer with high doping concentration, which has been deposited onto the substrate. The high doping is necessary to change the resistance temperature coefficient from negative (typical for silicon) to positive. Next to this light-sensitive structure there is a waveguide, which connects it with a grating intended for incoupling radiation in later experiments (Figure 2.10). Irradiation of the material heats up the doped wire and, as it will be shown in section 4, induces an increase of resistance due to more frequent collisions of the charge carriers.

2.2.2. P-N diode

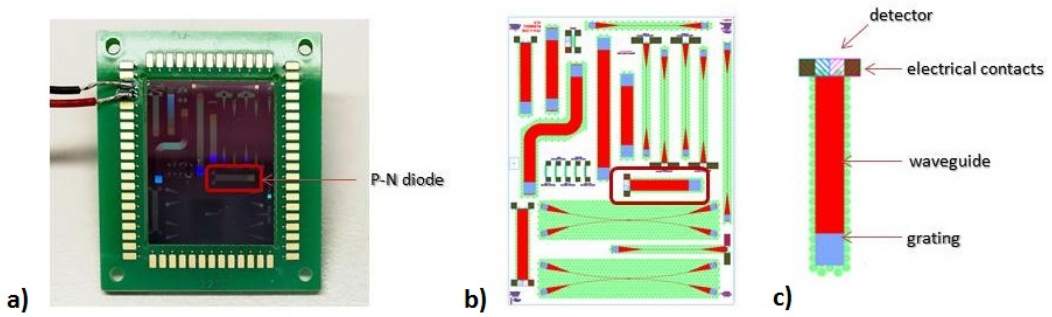

Figure 2.11.: a) Framed chip with P-N diode. b) Layout image of chip with diode detector. c) P-N diode.

Our second candidate is a P-N diode, but not used as described in section 2, working as a photovoltaic-based detector, but as a thermal detector. That's because the bandgap of silicon, which is at room temperature about 1.12 eV, is too large to induce a photovoltaic effect by infrared radiation. In practice this is a boron and phosphorus doped polysilicon P-N junction located in proximity of a waveguide with a grating on the other side. The waveguide structure is analogous to that facing the polywire. But in contrast to this, in the case of the diode the opposite happens when irradiated: The resistance decreases and the current flow increases. This happens because in a heating process from room temperature to about 150 °C (for the Si-diode) charge carriers are generated, thus increasing the current flow. For higher temperatures the characteristic curves drift to lower forward voltages (Figure 2.12). This happens because of decreasing internal resistance due to generation of a higher intrinsic carrier concentration. This reduces the bandgap, so the "turn on" voltage is reduced. A similar effect can be observed on the reverse bias as well. However, at large bias voltages (higher currents) the temperature coefficient becomes positive (reduction in carrier mobility induces an increase of resistance).

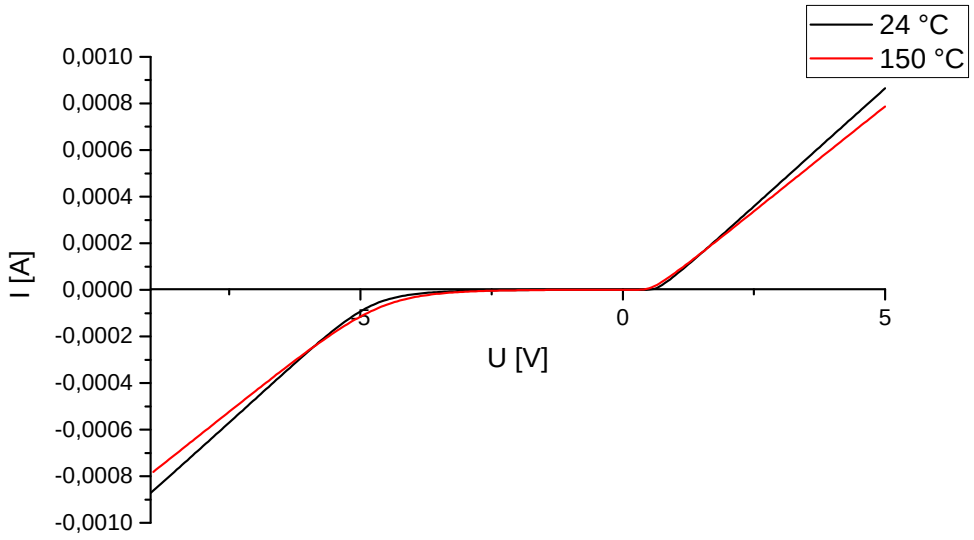

Figure 2.12.: Typical characteristic U-I curves of our P-N diode detector, measured at 24 °C and 150 °C.

2.2.3. Vertical-cavity enhanced detector (VERD)

As discussed in section 2.1.1, the VERTE is an emitter structure for mid-IR radiation, which was first proposed by I. Celanovic et al. [19] and further optimized for the wavelength range around 4.26 µm, at an operation temperature of 800 Kelvin, within this project. The 4.26 µm wavelength corresponds to the center of the carbon dioxide absorption band. [18] [31] [32] Based on Kirchhoff's radiation law, which says "a good absorber must also be a good emitter and vice versa", it seemed obvious to investigate the VERTE for its detection characteristics. From now on the absorption-based detector is called vertical-cavity enhanced detector (VERD) and is the main subject of this master thesis. One has to consider, however that the structure was optimized for emission at 800 K, but as a detector it should work at room temperature, what induces significant changes in emissivity (thus absorption) of the material. Parts of this project have been presented on the Eurosensors conference 2018 in Graz and are summarized in the associated paper. [33]

The VERD is composed of a thin dielectric cavity sandwiched between a one-dimensional photonic crystal (Bragg reflector) of alternating silicon and silicon dioxide layers on the front side and a thin reflective silver mirror on the backside (Figure 3.6), deposited onto a Si substrate. By placing the silver layer at the edge of the cavity, it fulfills several tasks: It forms the cavity, works as highly reflective, slightly absorbing mirror and it is used as

active device structure for read out, by detecting the cavity enhanced radiation in form of changes of the average device temperature.
Incident radiation at first has to pass the multilayer stack, consisting of alternating layers of materials with high and low refractive indices, $n_H = 3.55$ for Si and $n_L = 1.38$ for SiO_2. The layers can be fabricated by various vapour deposition processes, as discussed in 3.1. The effect of the layer stack on incident electromagnetic radiation can be derived using Maxwell equation.
If one takes a look at a homogeneous, isotropic, dielectric and non-magnetic medium and the one-dimensional case of an electromagnetic field only propergating in z-direction, the wave equation is given by

$$\frac{\partial^2 E}{\partial z^2} - \frac{\varepsilon}{c^2}\frac{\partial^2 E}{\partial t^2} = 0 \tag{2.5}$$

where c is the vacuum speed of light and ε is the (complex-valued) permittivity. Equation 2.5 is satisfied by

$$E = E_0 \cdot e^{-i(\omega t - k_z z)} \tag{2.6}$$

if k_z and ω obey to the dispersion law

$$k_z(\omega) = \varepsilon\frac{\omega}{c} \tag{2.7}$$

for angular frequency ω-dependent z-component of the wave vector k_z. Using this equation in 2.6 gives refractive index and extinctions coefficient as result. The detailed derivation can be found in reference [34]. Definition of extinctions coefficient

$$k = \mathrm{Im}(\varepsilon^{1/2}) \tag{2.8}$$

and refractive index

$$n = \mathrm{Re}(\varepsilon^{1/2}). \tag{2.9}$$

Further we define the complex refractive index as

$$\boldsymbol{n} = n + \mathrm{i}k. \tag{2.10}$$

[34]
By assumption of normal incidence of radiation ($\alpha = 0$), electromagnetic waves are partially reflected at transitions between materials with different refractive indices n_1 and n_2 according to Fresnel equation

$$r = \frac{n_1 - n_2}{n_1 + n_2} \tag{2.11}$$

At boundaries between materials with low and high refractive index a phase jump of π is happening. If the thicknesses of various layers are

$$d = \frac{\lambda_0}{4n_{1,2}} \tag{2.12}$$

where λ_0 is the vacuum wavelength of the desired radiation, you get destructive interference in reflection and constructive interference in transmission. Assuming an ideal Bragg reflector, the maximum reflectivity can be calculated by

$$R_{\mathrm{Bragg}} = \left(\frac{1 - \frac{n_{\mathrm{out}}}{n_{\mathrm{in}}} \left(\frac{n_{\mathrm{L}}}{n_{\mathrm{H}}} \right)^{2M}}{1 + \frac{n_{\mathrm{out}}}{n_{\mathrm{in}}} \left(\frac{n_{\mathrm{L}}}{n_{\mathrm{H}}} \right)^{2M}} \right)^2 \tag{2.13}$$

where n_{in} and n_{out} identify the refractive indices of entrance and outlet medium, which are bordering the Bragg mirror, M is the number of layer pairs, n_{L} and n_{H} low (L) and high (H) refractive index of alternating layers (Figure 2.13) [35].

Apart from dependence of the refractive index from wavelength of the propagating light (dispersion)

$$n = \frac{\lambda_0}{\lambda} = \frac{c}{v} \tag{2.14}$$

where λ_0 is the vacuum wavelength, λ the wavelength in matter, c the vacuum speed of light

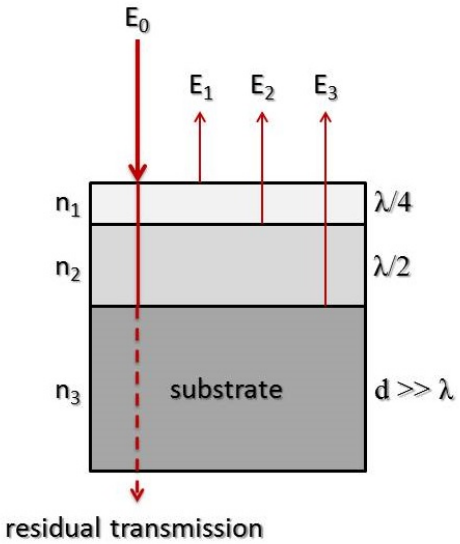

Figure 2.13.: Schematic of working principle of a Bragg (dielectric) mirror (in style of [35]).

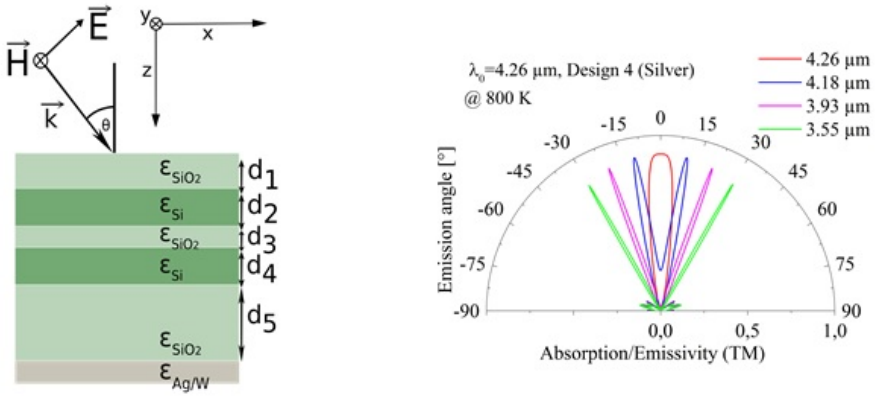

Figure 2.14.: Decreasing wavelength due to angular distribution of incident light. Left picture shows radiation incidence under angle θ, right polar plot shows wavelength shift at different angles.

and v the speed of light in matter, n depends also on the material and its microscopical structure. Therefore, the value of n depends on the details of the fabrications processes. Sputtering yield and residual gas pressure within the deposition equipment influence the layer density. A higher density gives lower extinction k and higher refractive index n.

The Bragg reflector of the VERD is designed for a central wavelength of 4.26 µm and followed by a SiO_2 half wave cavity, which acts as a Fabry Perot interferometer. If the

radiation does not hit the detector perpendicularly, but tilted at a certain angle, the structure shows absorption at lower wavelength values (2.14). Considering the phase shift $\Delta\phi$ for a Fabry-Perot interferometer, which is about

$$\Delta\phi = \frac{4\pi}{\lambda} nh\cos\theta' \tag{2.15}$$

where the variables are defined in Figure 2.15, this can be described as follows.

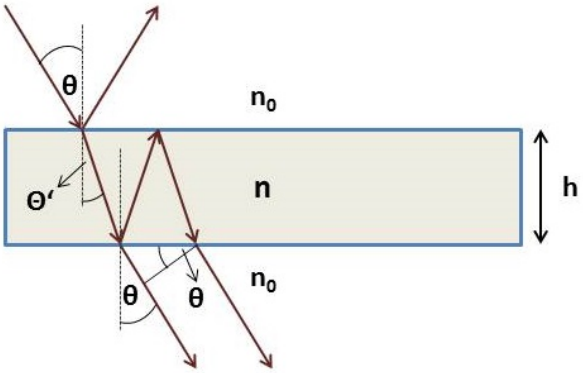

Figure 2.15.: Scheme for explanation of beam path through a Fabry-Perot interferometer. h is the layer thickness, n_0 the refractive index of the surrounding area, n the refractive index of the layer, θ the angle of incidence, θ' the angle of refraction.

For an interference maximum, the phase shift must be $\Delta\phi = 2\pi \cdot m$. If one equates this with equation 2.15, it gives

$$2\pi = \frac{4\pi}{\lambda} nh\cos\theta' \tag{2.16}$$

and further

$$\lambda = 2nh\cos\theta'. \tag{2.17}$$

If θ increases, also θ' gets larger, according to Snell's law, and induces a decrease in resonant wavelength. [35]
Within the cavity a high electromagnetic field intensity is achieved, depending on the cavity Q factor. The Q factor, resonant cavity quality factor, is defined as

$$Q = 2\pi f_r \cdot \frac{\text{energy stored in the cavity}}{\text{power loss}} \tag{2.18}$$

where f_r is the resonant frequency [36]. It can be calculated from two seperate terms, the internal quality factor related to the power dissipation within the resonant structure and the external quality factor, which depends on the coupling of the resonator to the surrounding environment. A high-Q resonant cavity enhances the amplitude of the electromagnetic field through interference of multireflected beams. This further leads to a higher energy absorption by the active device and finally to a larger response. The demand on high reflectivity and quite low absorption of the silver mirror is necessary to avoid swallowing of radiation and further fall off of responsivity. The absorption of the incoming radiation leads to an increase in temperature which induces a change of resistivity and can be read out by electical contacts, connected to the silver layer. [37] [38]

2.3. Characteristic values

In order to be able to compare the three different detector concepts at the end of this work, characteristic values were determined, namely sensitivity, responsivity and the noise equivalent power. The nomenclature is not always the same within different communities, therefore these concepts are introduced below.

Sensitivity The sensitivity refers to the minimum signal that can be measured by the detector, therefore it is related to the intrinsic noise of the detector as:

$$sensitivity = 3 \cdot \sigma \tag{2.19}$$

where σ is the standard deviation of the noise signal.
In our case it has to be considered, that also additional noise, due to cable connections and the setup is measured.

Responsivity Responsivity refers to the signal magnitude per power of the incident radiation. The responsivity may change over the measurement range if the detector response

is not linear.

Noise equivalent power (NEP) For concrete comparison of different investigated detectors, we calculated the noise equivalent power (NEP) for each of them. This is a factor for measure of sensitivity of photodetectors. It can be mathematically determined by

$$\mathrm{NEP} = \frac{3 \cdot \sigma}{\sqrt{B}} \tag{2.20}$$

where B, the bandwidth, is defined as

$$B = \frac{1}{2 \cdot t_{\mathrm{avg}}} \tag{2.21}$$

with
t_{avg} ...average integration time.
For example, for t_{avg}=0.02 s, corresponding to 50 Hz mains frequency, that leads to a bandwidth of 25 Hz. σ is defined as the standard deviation of the intrinsic noise level of the respective detector. So, finally it can be said, the NEP gives the amount of incident light in units of $\mathrm{W/Hz^{0.5}}$, corresponding to a signal to noise ratio of 1. Summarizing one can say, a smaller NEP corresponds to a more sensitive detector. [39]
If one takes a look into technical literature, typical NEP values for bolometer detectors are on the order of 10^{-9} $\mathrm{W/Hz^{0.5}}$. To compare with these values, we have to keep in mind, that our structures are not fully integrated yet, and they are measured by setups not yet optimized in terms of noise reduction. So what we measure and calculate is more or less the detectors NEP, in consideration of the non optimal measurement conditions.

Chapter 3.

Materials and Methods

The aim of this section is to give a short explanation of the methods that were used to fabricate and characterize the detector structures. All of them were fabricated at Infineon Technologies Austria AG. Wire bonding and characterization was conducted at CTR AG.

3.1. Microfabrication methods

Several thin film technologies can be used for deposition of thin layers on a Si substrate. One roughly can differentiate between two basic procedures: Chemical and physical vapor deposition.

3.1.1. Chemical vapor deposition

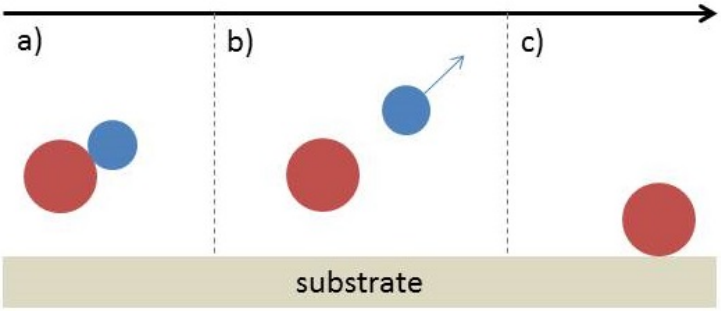

Figure 3.1.: Schematic representation of a CVD process. a) The precursor gas is brought into the reaction chamber, b) through energy supply the gas gets dissociated and radicals (red) are formed, c) radicals bind to surface by chemical reactions.

Chemical vapor deposition (CVD) ist one of the most common coating methods. It enables the coating of a variety of metallic and ceramic materials. The coating material is brought into a reaction chamber in form of a gaseous precursor, wherein it is mixed with so-called carrier gases. The precursor, which contains the actual reactant, then gets dissociated by energy supply. The resulting radicals then undergo chemical reactions with the substrate to be coated (Figure 3.1). The gas molecules flow past the substrate and the radicals bind to it, through which a solid phase is deposited. By addition of thermal or radiation energy, the substrate temperature is adjusted to facilitate chemical reactions with the coating material. [40]
The process calculation has to include all possibilities of reactions, homogeneous gas phase reactions should not take place due to dust formation, what affects the layer formation. Monitoring the relocation of reaction equilibrium and change of process parameters, e.g. the temperature, is necessary to predict whether thin film deposition is taking place. CVD layers grow around 1 µm per minute on average, what depends on several factors like reactand diffusion velocity, reactand adsorption on substrate surface, desorption of reaction products etc. [41]
There are several types of CVD processes, two of them are described more in detail.

Low pressure CVD (LP-CVD) Low pressure CVD is a process used to deposit layers in a wide range of thicknesses. Values from a few nanometers to several micrometers are easily reachable. This method is mainly used to deposit polysilicon, thick oxides, doped oxides, nitrides and other dielectrics. Typical values for the working pressure are between 10 and 1000 Pa. Depressurization leads to smaller mass transport velocities, as compared to other CVD precesses. This induces better uniformity and homogeneity of the deposited films. Other advantages of this technique are high purity, simple handling and high reproducibility. [42]

Plasma-enhanced CVD (PE-CVD) Plasma enhanced chemical vapor deposition is the standard method for deposition of amorphous silicon layers, silicon dioxide and several other silicon compounds. Therefore, a plasma, which is a partially ionized gas with a high proportion of free electrons, is added to the reaction chamber. Compared to other CVD processes, where the gaseous molecules of the precursor are dissociated by thermal energy supply and, therefore, all particles are quite of the same temperature, in cold plasmas the electrons have a much higher temperature than the remaining gas particles and ions. Operating temperatures between 100 and 400 °C are achievable. The electrons then release

their energy by collisions to the reaction gas and dissociate the molecules in order to induce the layer deposition. To excite and sustain the plasma state, a voltage has to be applied by two electrodes. Main advantages of PE-CVD are low operating temperatures compared to LP-CVD (usually 600 - 1100 °C) and high layer density. [43]

3.1.2. Physical vapor deposition

In physical vapor deposition (PVD) processes atoms of the coating material are deposited onto the substrate in vacuum by condensation, without any chemical reactions. One differentiates between several technologies, the two most common are described below. [44]

Sputtering When high energy ions hit the surface of a solid, neutral atoms, clusters, molecules or ions can be emitted. Such a process is called sputtering and several coating techniques rest upon that. In practice the coating material (target) and the sample, which has to be coated, are placed together in a high vacuum chamber. Further an anomal glow discharge between the target (source) as cathode and the substrate as anode has to be maintained, to activate an ion bombardment. When ions impinge on the target, various effects can appear: The impinging ion can be reflected at the target surface, generate secondary electrons, can be implanted into the target lattice or it transfers part of its energy to lattice atoms. By induced collision cascades, some atoms are backscattered to the surface (Figure 3.2). If their energy is higher than the surface binding energy, they can exit the lattice and ideally move towards the substrate surface. Onward they get either reflected or transfer enough energy to the substrate, to get loosely bound as adatoms. Further the adatoms diffuse over the substrate surface until they either desorb or form a stable nucleus. Another possibility is to condense by attachment to already existing nuclei. Those are growing to islands and finally forming a continous thin film of coating material. The quality of the final layer depends on parameters like substrate temperature, gas pressure and sputtering yield.
The sputtering yield Y is defined as number of sputtered atoms j_{sp} devided by number of atoms impinging on substrate surface j_{i}

$$Y = \frac{j_{\mathrm{sp}}}{j_{\mathrm{i}}} \tag{3.1}$$

where current j is the flow of atoms.

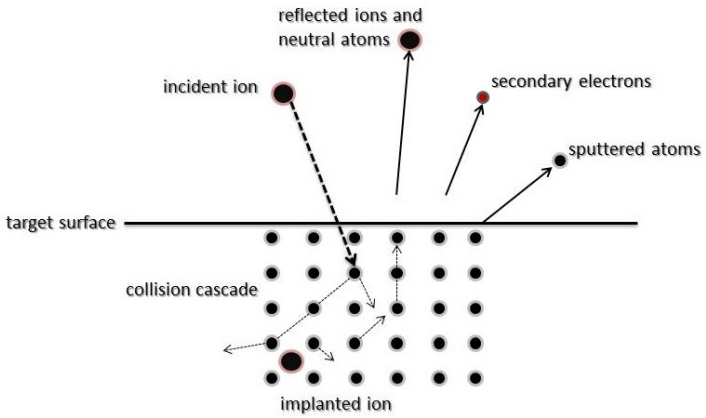

Figure 3.2.: Schematic representation of sputtering process. The incident ion gets decelerated within the solid target. Collision cascades are activated, further energy and impulse are able to turn back to the surface (in style of [45]).

The sputtering yield depends on target material, ion energy, ion mass and angle of incidence. The main advantage of sputtering technology is its universal applicability. Due to evaporation by impulse transfer and no thermal excitation, basically every substance can be sputtered. [46]

Evaporation In this process, the coating material is put into a vacuum chamber in an appropriate container, mostly a crucible, and evaporated by energy supply until heated to sufficient temperatures. Thermally released atoms or molecules then form a coating on the substrate and the sorrounding walls of the equipment. High vacuum is necessary for achieving straight trajectories to form sharp edges and prevent the coating particles from collisions with residual gas atoms, when vaporizing masks. The heating process can be affected by several methods, the most popular works by irradiation through an electron beam. This technique is avoiding reactions between the melt and the crucible because of a water-cooled copper reservoir. Also advantages like high coating rates and purity made electron beam evaporation to an essential universal method for fabrication of high quality thin films. A schematic of an evaporation plant is shown in figure 3.3.

A substrate heater is required to achieve clearly defined layer properties. For this purpose

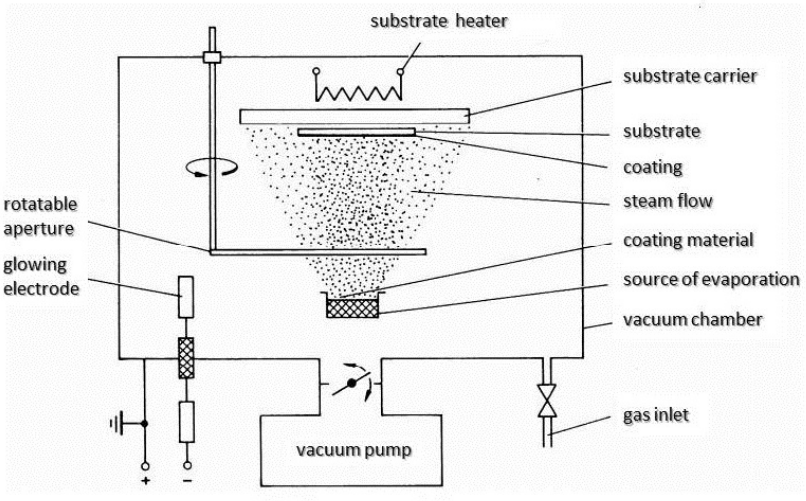

Figure 3.3.: Schematic of evaporation plant [46].

the substrate temperature has to amount up to a few hundred degrees celsius. [46]
One of the most important evaporation techniques for fabrication of well-defined thin films, especially within the semiconductor industry, is the so-called molecular beam epitaxy (MBE). It describes the oriented growth of a certain layer onto a crystal surface of a substrate. [47]

3.1.3. Lithography

Lithography is basically an essential process for fabrication of a semiconductor device. Thus, according to the layout, design information is defined on the silicon wafer. A radiation-sensitive layer, the photoresist, is applied onto the wafer, cured and then exposed to ultraviolet light. The resolution, and thus the limitation of the miniturization of the device, is determined by the wavelength of the radiation used. After exposure, the postbaking is done to completely desiccate the resist and to improve chemical resistance. Subsequently, the photoresist is developed and the irradiated or non-irradiated part, depends on whether it is positive or negative processed, removed according to the mask. [48]

3.1.4. Etching

The etching process serves to remove certain layers from the silicon substrate or to remove parts of the material itself (e.g. according to the lithographically created mask pattern). There are basically two different methods: wet-chemical or dry, plasma-assisted etching.

An important property of wet-chemical etching is its isotropic behavior. Although this process has widely different etching rates for different material (e.g. mask and substrate), the isotropy causes undercutting of the mask and limits the resolution to about 1 micron (Figure 3.4). Therefore this method is mainly used for non-critical etching steps. However, there are also anisotropic wet-chemical etching processes. Among others, concentrated KOH is used for anisotropic Si etching. Figure 3.4b shows anisotropic Si etching, where the more stable 111 planes, compared to 100 and 110 Si crystal planes, act as an etch stop.

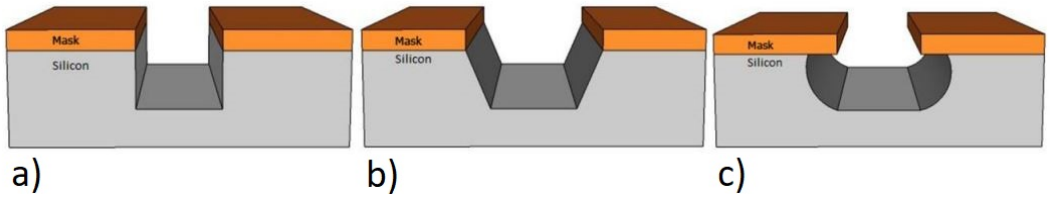

Figure 3.4.: Difference between a-b) anisotropic and c) isotropic etching. [49]

Dry etching processes are the most important pattern transfer processes at the current state of microfabrication. They are usually characterized by high anisotropy and have very accurate pattern transfer, also for small mask structures. The operating principle is based on plasma chambers, in which gases are dissociated to perform the surface reaction, catalyze or simply remove the material by physical processes. Another possibility is the use of ion beams, called reactive ion etching (RIE), which is a combination of physical and chemical mechanisms. In addition, high resolutions can be achieved with this method. The etching characteristics depend mainly on the pressure within the plasma chamber: lower pressure provides better resolution. [49] [50]

3.2. Microfabricated structures

Within this section the fabricated detector structures are described. For all structures, the fabrication was performed by Infineon Technologies Austria AG, before the start of this thesis.

3.2.1. Doped polysilicon wire

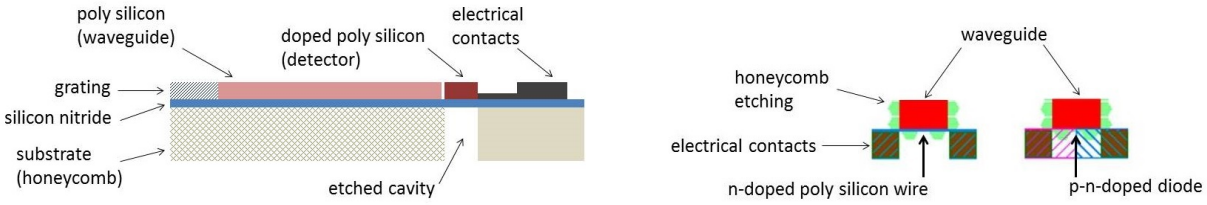

Figure 3.5.: Scheme of the layer structure of polysilicon wire and diode detector. Left picture shows a lengthwise cross section, the right picture shows the structure from the top. The layer structure is identical, but the doping of the sensitive area is different: n doping for the polysilicon wire, p-n doping for the diode.

The polysilicon detector is placed in front of a waveguide that has a grating on one side, through which the radiation is coupled into the waveguide. The sensitive area is a wire of doped polysilicon, connected to two electrical contacts for read out (Figure 3.5).
For that, first a 575 nm SiO_2 layer is deposited onto the silicon substrate by low pressure CVD. After an annealing process at 900 °C, a 140 nm thick silicon nitride layer is applied, which later should form the membrane for a free standing detector. Further, an amorphous silicon layer is deposited also by low pressure CVD and annealed to obtain a 660 nm poly silicon film. Subsequently patterns are created by lithography processes, to structure the detector and the grating by etching. After removing the photoresist, doping is performed by phosphor implantation. The dose used is about $3.6 \cdot 10^{15}$ cm^{-2}. After implantation, the wafer is returned to the oven to heal defects within the crystal lattice and thermally activate the implanted area. After a few more etching and cleaning processes to remove intermediate protective layers and to ensure the purity of the surface, finally the substrate under the polywire is completely removed by reactive ion etching and the polywire rests only on the silicon nitride membrane. So it is thermally isolated. Also the substrate under the waveguide is partially etched away and only thin webs in form of a honeycomb pattern remain.

3.2.2. Diode

The layer structure and fabrication of the diode is analogous to the doped polysilicon wire detector, except the implantation process. This structure gets implanted with boron and phosphor, to obtain a P-N junction (Figure 3.5).

3.2.3. VERD

For the VERD first a 0.37 µm thick SiO_2 layer is deposited onto the silicon substrate by low pressure CVD, followed by a 0.3 µm Si layer, deposited at lower temperatures by PE-CVD. Further a 0.77 µm SiO_2 layer and another 0.3 µm Si layer are attached. Then the SiO_2 half wave cavity, which has a thickness of 1.5 µm was created (Figure 3.6).

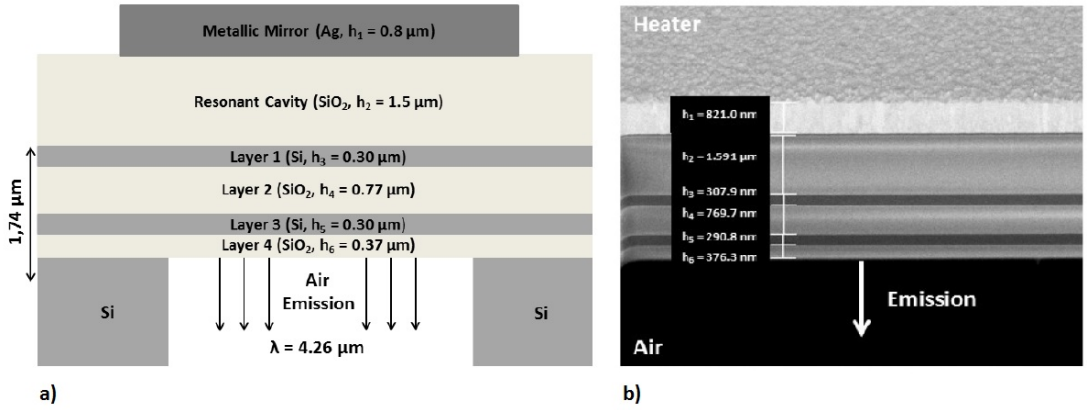

Figure 3.6.: Schematic of the VERTE structure (a) and an example FIB cross section through the fabricated device indicating the individual layer thicknesses (b). [18]

After sputtering a silver layer onto the stack of alternating Si and SiO_2 layers, the metal is structured to obtain a meander based heater and further connected to electrical pads. The meander structures were fabricated in different shapes, circular and rectangular, and different sizes (Figure 3.7). For thermal isolation the silicon substrate below the heater is again removed by reactive ion etching.

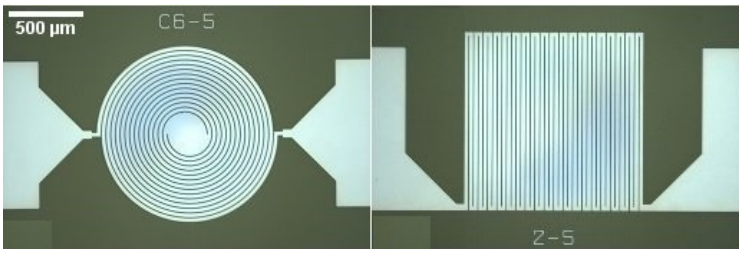

Figure 3.7.: Images of two different shapes of the silver meander structure of the VERD, which are connected to electrical pads for the read out. Each of the two shapes was fabricated in several different sizes.

3.3. Printed circuit boards (PCBs)

PCBs are boards of electrically insulating materials that are used as carriers for electronic components. Via conductive tracks that are located on such a board, mechanically fastened devices can then be connected. To contact them with the tracks, the components are soldered either directly or indirectly via cable connections to electrical pads. Another method for contacting an electronic device with the pads is by wire bonding.
In this work, the chips with the respective detector structures were glued in PCB frames and contacted by wire bonding (figure 3.8).

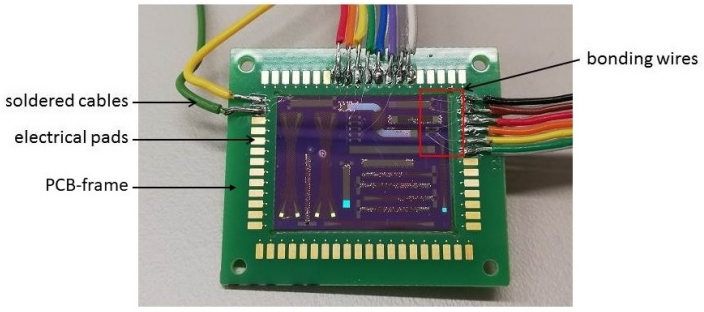

Figure 3.8.: Chip on PCB-frame with wire bonded detector-structures.

3.4. Wire bonding

Wire bonding is the most common technique for contacting not fully integrated semiconductor devices, or to connect certain structures to measurement devices within the research process. One distinguishes between three fundamental bonding methods: thermocompression (TC)-, thermosonic (TS)- and ultrasonic (US)- bonding.

As the name already indicates, the first two concepts are based on thermal energy and pressure action. The bonding wires used are usually gold, what provides advantages like being non-oxidizing and very good thermomechanical ductility. Around 300 °C have to be applied at the connection spot, which has to be free from dust particles or other contaminants to achieve best possible adhesion (TS-bonding is somehow an advancement of TC-bonding and requires lower temperatures of about 120 - 200 °C). Such high temperatures could damage the PCB and lead to electrical disfunction.
Compared to the two methods discussed above, US-bonding, which was used for this work, operates without external thermal energy supply, so no thermal stress occurs. The utilized tool was the Model 4526 from Kulicke and Soffa. Relative movement with a frequency in range of the ultrasonic regime and the exertion of force (in scale of 10^{-2} Newton) lead to performance of mechanical work, dislocation motion and generation within the bonding wire. The result are metallic bonds between the join partners. That way, welded micro areas are created. [51]
For electrical characterization chips with the detector structures have been glued into insulated PCB frames with metallic pads on them. The detector structures have been wire bonded to the pad contacts on the frame and cables were soldered to the metallic connection.

3.5. SEM/ FIB analysis

Scanning electron microscopes (SEM) have around 40 times better point resolution than conventional light microscopes, down to 0.005 µm. In addition 800 times better depth of field is reachable.
The operating principle is based on electrons accelerated up to 40 keV, which scan the sample surface in the form of a focused beam. Interaction with the surface leads to generation of secondary electrons, backscattered electrons and others. With help of suitable detector systems, this information can be used to create an image of the surface. [52] The microscopy technique with focused ion beams, which is very similar to scanning electron microscopy (SEM), got more and more popular in microstructuring, surface and thin film characterization within the last few years. Nowadays it is an essential routine procedure in semiconductor industry and also other branches like biomedical engineering.
The central element of such FIB investigation instruments is a liquid metal ion source, usually gallium, of high stability and durability. Gallium provides low volatility, vapour

pressure and a low melting point (29.8 °C). The working principle is based on a heated gallium reservoir, from where the ions flow to the tip of a tungsten pin. By applying a voltage between the tungsten pin and the subjacent extraction aperture an electrical field at around 1000 V/m is generated. If the electrostatic forces are higher than the binding energy, this leads to continuous field emission of gallium ions. Further the ions are accelerated up to several keV and focussed onto the test sample by electrostatic and magnetic lenses. The beam is scanning the sample surface, secondary electrons are released, detected and allow to create an illustration of the topography and composition of the surface. Furthermore the intensity of the transmitted and the reflected beam part can be measured.
FIB devices are not just applicable for surface structure investigation and layer thickness measurements etc. but also for inducing surface sputtering actions and material removal (e.g. milling). In modern concepts FIBs are coupled with SEMs. With those so called cross-beam systems it is possible to evaluate and work on certain spots of a sample simultaneously. [53]

3.6. Experimental characterization of detector structures

3.6.1. Equipment

- Keithley 2450 SourceMeter
  The Keithley 2450 is a modern source meter unit allowing to apply a voltage and simultaneously to measure the current or the ohmic resistance. Measurements are feasible with 0.012% basic accuracy and signal data can be read out by the Keithley KickStart Software.

- Stanford SR830 DSP Lock-in Amplifier
  If signals are on the order of a magnitude so that they are easily superimposed by noise or other interference, lock-in (LI) amplifiers are used. If an electrical system is excited with a well-defined frequency and only its response is examined, then it is possible to amplify the signal with an LI amplifier and filter it at the same time.
  In this work we excited the respective detector structures by modulated infrared radiation through a interposed chopper and passed its frequency over to the LI amplifier as reference signal. So it was possible to inhibit noise and unintentional drifts.

- Newport 919P Thermopile powermeter
  With this sensor power measurements for continous wave (CW) and pulsed lasers are

practicable within a maximum power range up to 3 W.

- MIRcat 1100 U2 QCL
  The MIRcat 1100 U2 is a high-speed tunable multi-quantum cascade laser system, developed and fabricated by DRS DAYLIGHT Solutions. The QCL is tunable for wavelengths within the mid IR regime, in range of 3.95 µm to 4.35 µm. It can be operated in CW or in pulsed mode, where maximum power values of around 220 mW can be reached. In pulsed mode the QCL is able to work at pulse rates up to 100 kHz with a pulse width from 20 to 500 ns.

3.6.2. Optical characterization of the VERD

A very important factor for such thin film structures is the reproducibility with sufficient accuracy. That is only one of many reasons why it is essential to examine thin films relating to thickness, optical properties like refractive index etc.
In our case we are interested in an accurate characterization of the absorption spectrum of the produced structures. This characterization was performed by Fourier-transform infrared (FTIR) microscopy.

Fourier-transform infrared (FTIR) spectrometer (LUMOS)
Modern devices for infrared absorption or transmission measurement usually use Fourier-transform spectrometer. In contrast to conventional grating spectrometers, with FTIR spectrometers a much more accurate resolution of the investigated spectrum is achievable. The most common FTIR spectrometers are based on a Michelson interferometer, shown in Figure 3.9. An infrared radiation source emits light in the direction of a beam splitter, which splits it into two sub-beams. Let's first consider the case of a monochromatic beam with wavelength λ. The sub-beams are then reflected by two different mirrors and meet again at the beam splitter, where they recombine and further propagate to a detector. One of the mirrors is fixed, the other moveable. If both mirrors are set to have the same distance to the beam splitter (d=0, where d is half the difference of the light paths), both sub-beams return the same way until they hit the detector. If the moveable mirror is displaced, then one of the beams must have a longer path length of $\delta = 2d$. At the detector, the two partial beams interfere. If $\delta = 0$ or $\delta = n \cdot \lambda$, where n is an integer, then the beams are in phase and constructive interference is happening. Therefore the intensity at the detector corresponds to the intensity of the source. Is $\delta = (n+1) \cdot \frac{\lambda}{2}$, the two beams eliminate each

other, destructive interference is happening. If the movable mirror is moved over a distance during a measurement, the intensity pattern at the detector corresponds to a cosine function.

$$I(\delta) = \frac{I_0}{2} \cdot \left[1 + cos(\frac{2\pi}{\lambda}\delta)\right] \tag{3.2}$$

where I_0 is the source intensity. The intensity as a function of the optical path difference δ gives an interferogram, whose period depends on the wavelength λ of the light.
If now a non-monochromatic source is considered, the sum of the monochromatic interferograms can be calculated as an integral:

$$I(\delta) = \int_{-\infty}^{+\infty} d\nu S(\nu) \cos(2\pi\nu\delta) \tag{3.3}$$

where $S(\nu)$ is the spectrum of the light source and $\nu = \frac{1}{\lambda}$. With Fourier transformation it is possible to calculate back the spectrum $S(\nu)$ from the interferogram $I(\delta)$ by use of an inverse, which is expressed by:

$$S(\nu) = \int_{-\infty}^{+\infty} d\delta I(\delta) \cos(2\pi\nu\delta) \tag{3.4}$$

[54]
By knowledge of the source spectrum, it is then possible to put a sample between the beam splitter and the detector and measure either the light reflected from the sample or the transmitted light. So it is possible to obtain the reflection and absorption spectra of the sample, respectively.

The FTIR microscope, used within this work, is the LUMOS microscope from Bruker. This tool has a special lens, an 8X Cassegrain objective, with a numerical aperture

$$NA = n * \frac{\sin\alpha}{2} \tag{3.5}$$

of 0.6 for focusing the infrared radiation on the sample (Figure 3.10). As a result, the radiation does not impinge on the sample vertically, but tilted at a certain angle. This affects absorption measurements of the VERD structure, described in 2.2.3. Since no more detailed data from Bruker corporation is issued, we took typical values for divergence

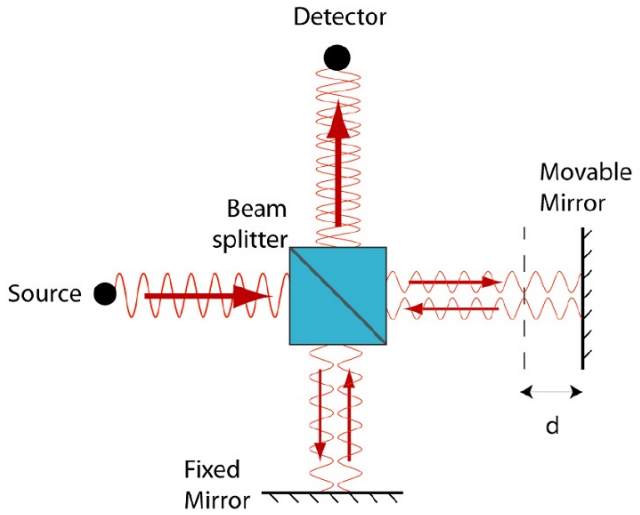

Figure 3.9.: Schematic representation of a Michelson interferometer. [54]

angles for Cassegrain/ Schwarzschild objectives of literature [55]. Further a Matlab script was programmed (see section A.1), with which we could fit the simulation data to the measurement data by simple manual iteration for standard deviation σ of the Gaussian intensity profile for the radiation beam, which defines the full width at half maximum. More detailed information in section 4.3.

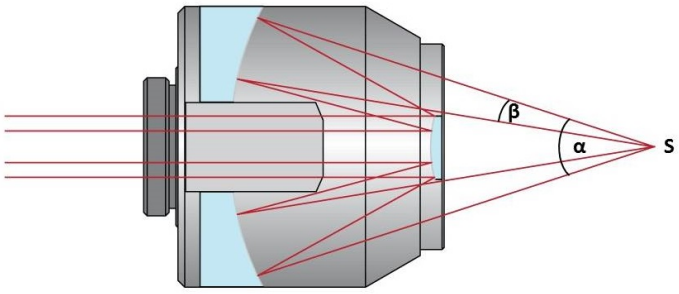

Figure 3.10.: Schematic representation of a beam path within a Cassegrain obejctive (reprint from [56]).
S: sample, α: aperture angle, β: divergence angle

3.6.3. Electrical characterization

First step of characterization procedure was about investigating the heating characteristics of the polysilicon wire and the diode. For the VERD structure this was already done

previously and the measurement values have been taken over for further investigations. For this, chips with the respective structures have been inserted into a customized stainless steel chamber, connected to a calibrated heating system. The structures, one by one, have been wire-bonded to integrated platinum pads of the heating cell, which was further connected to a source meter unit. The individual chips have then been heated in several steps from 25 °C to 500 °C. For each temperature the resistance, or the current for the diode, were measured with the source meter for voltages from -9 to 5 V. Such calibration measurements allowed to determine the proportionality between the average device temperature and change of resistance for the poly wire and between the average device temperature and the change in current at a fixed bias voltage for the diode. Such proportionality is further used to express responsivity as a function of the average device temperature.
For producing statistics and checking the repeatability, measurements have been repeated on four chips from different wafers for each structure.

3.6.4. Responsivity and sensitivity characterization

To characterize the response of the different detectors to mid-IR radiation, light from the MIRcat QCL was used. For this purpose, a pre-existing optical setup [23] was used and further adapted. The optical setup is shown in Figure 3.11. It consists of the MIRcat quantum cascade laser (1), an optical system of two gold mirrors and a ZnSe objective to couple the laser beam into an InF_3 optical fiber (Figure 3.12), through which the light propagates towards the detector structures. Both endings of the fiber and also the holder system for the chip are mounted on 3D-stages, which can be adjusted by micrometer screws, allowing an optimum alignment.

The measurement setup to characterize the VERD structure slightly deviated from that for the doped polysilicon wire and the diode. While the laser beam for the polysilicon wire and the diode was directly coupled into the grating via the fiber (type: Thorlabs MF11) and then ran via the waveguide to the actual detector(Figure 3.13a), for the VERD it was first coupled into an optical system consisting of two identical lenses. The first lens collimates the divergent incident beam, the second focuses the radiation onto the detector structure, which is placed as best as possible in the focus of the lens, what was achieved by manual alignment (Figure 3.13b). For initial tests the chip with the detectors was mounted to a fixed rod, later the alignment was done by turning the micrometer screws of the 3D-stage to which the chip with the detector structures was mounted. While real time monitoring the

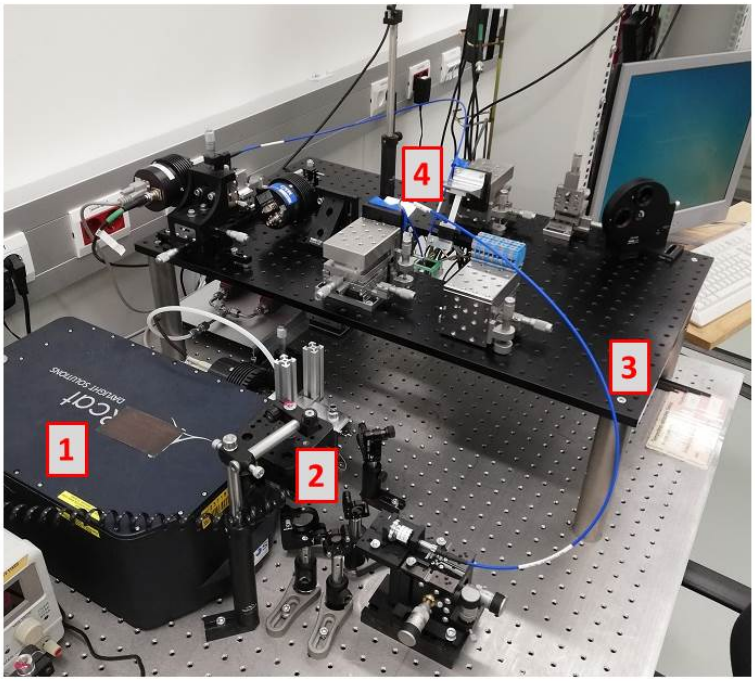

Figure 3.11.: Image of the measurement setup: 1 MIRcat QCL, 2 optical system for laser incoupling, 3 fibre, 4 holder system with mounted chip and fibre output.

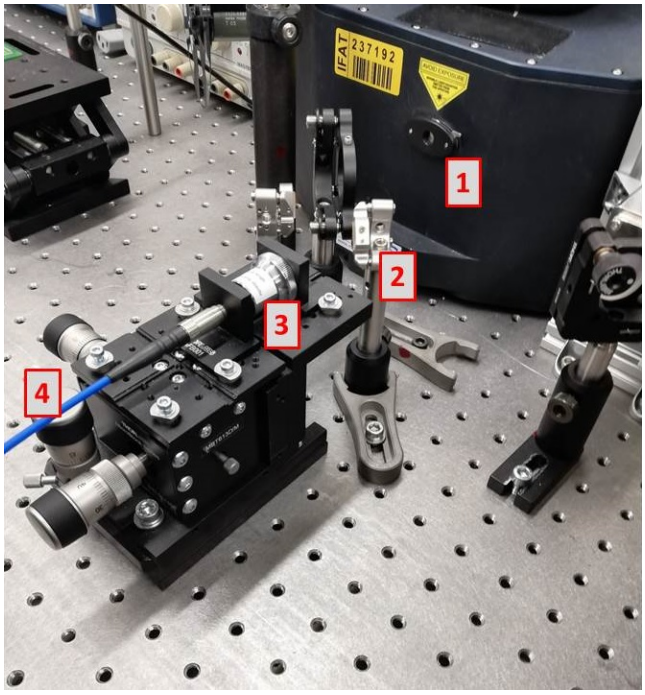

Figure 3.12.: Image of optical system within the setup for incoupling the laser beam into the fiber: 1 laser output, 2 mirrors, 3 incoupling objective, 4 fiber.

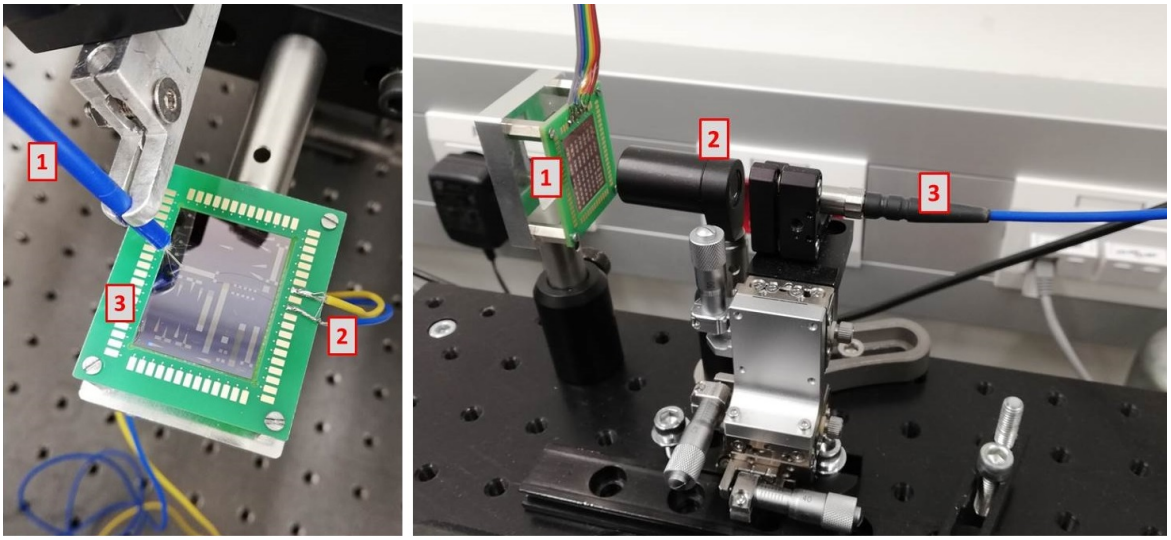

Figure 3.13.: a) Measurement setup for diode (analogous for polysilicon wire detector): 1 fiber, 2 soldered wires for connection with measurement device, 3 chip with respective detector structure on PCB-frame. b) Measurement setup for VERD: 1 chip with VERD structures on PCB-frame, 2 optical system, 3 fiber.

respective detector response to laser irradiation on the computer, connected to the source meter via the associated software, the screws were rotated until maximum amplitude of the signal was achieved.

As a reminder, laser irradiation leads to an increase of temperature, which can be read out as a change of resistivity for the poly wire and VERD or rather as a change of current for the diode. Previous calibration measurements (3.6.3) give the proportionality factors for recalculating the measurement values to uniform responsivity description by change of average device temperature.

Before we started with intrinsic characterization measurements of the detectors, we had to characterize the measurement setup.
First of all, we recorded the laser power as a function of the wavelength. For that we coupled the laser beam into the fiber and placed a thermopile powermeter in front of the fiber output. Then we set the laser current to 950 mA, tuned it to 3.95 µm and moved in certain steps through the whole range to 4.35 µm (Figure 3.14).
Maximum laser power is reached between 4.16 and 4.17 µm (2400 cm^{-1}). Also the influence of CO_2 absorption is visible in this graph. To avoid this effect, most measurements have been done at 4.17 µm, what corresponds to the laser maximum and is also out of the CO_2 absorption band.
Rather than using mid IR filters we used the current settings of the laser to control the emitted power, so further the laser power was monitored as a function of the laser current (Figure 3.15). This calibration measurements are necessary for subsequent normalization calculations. Notice, that this was done, before each measurement to account for small alignment changes.

For the diode and the doped polysilicon wire it must be taken into account that the laser radiation does not strike the detector directly, but is coupled via a grating into the waveguide, which leads to the detector structure. This causes losses and the power measured at the fiber output does not reach the detector. Calculations previously done by project staff showed that an average of 8 % of the power reaches the detector structure.

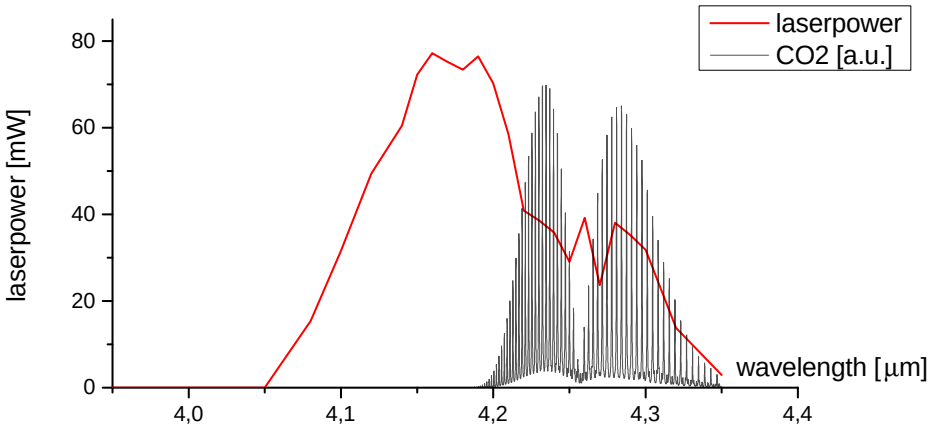

Figure 3.14.: Calibration measurements: laserpower as a function of wavelength compared to CO_2 absorption spectrum.

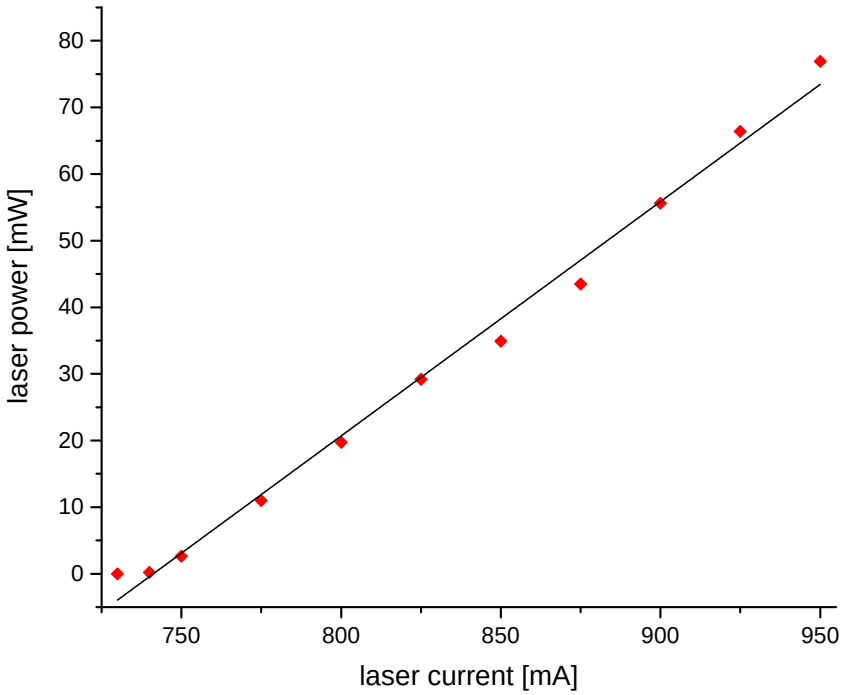

Figure 3.15.: Calibration measurements: laserpower as a function of lasercurrent and linear fit.

Chapter 4.

Results and discussion

In this chapter the results of our characterization measurements are presented and explained. At the end a comparison of all three detector structures should be set up to determine the best performing one.

4.1. Doped polysilicon wire

First, the structure was bonded and put into the heating chamber to determine the proportionality between resistivity and temperature change. Voltages from -9V to 5V in steps of 0.05V were applied and the ohmic resistance was measured with a source meter. The measured characteristic U-I-curve is shown in Figure 4.1. As expected, measurements show a linear trend of the U-I lines, according to Ohm's law. Next, the chamber was connected to the heating system and heated up from room temperature (here 27 °C) to 500 °C for investigation of response to temperature change.

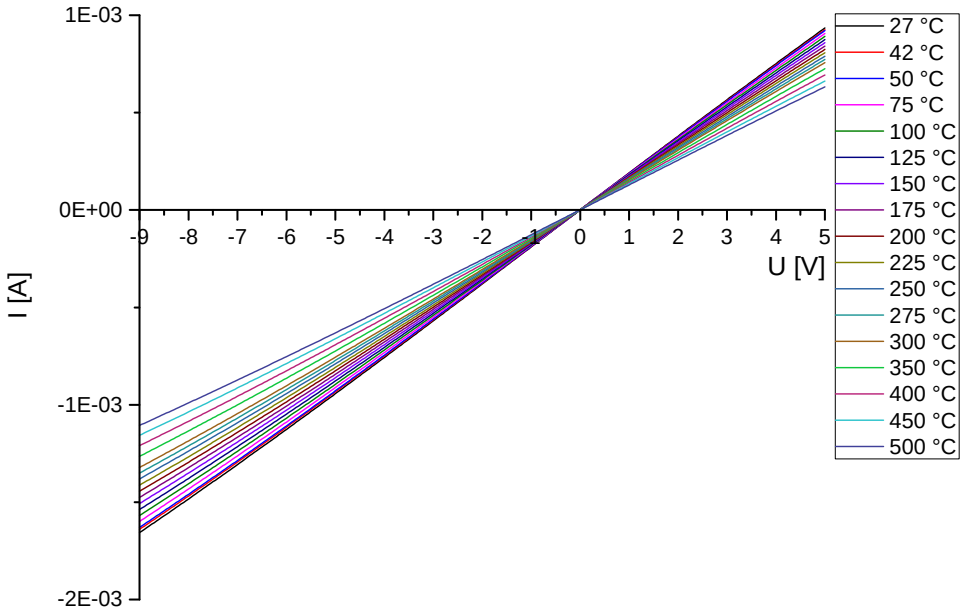

Figure 4.1.: Characteristic curves of doped polysilicon wire in dependence of temperature.

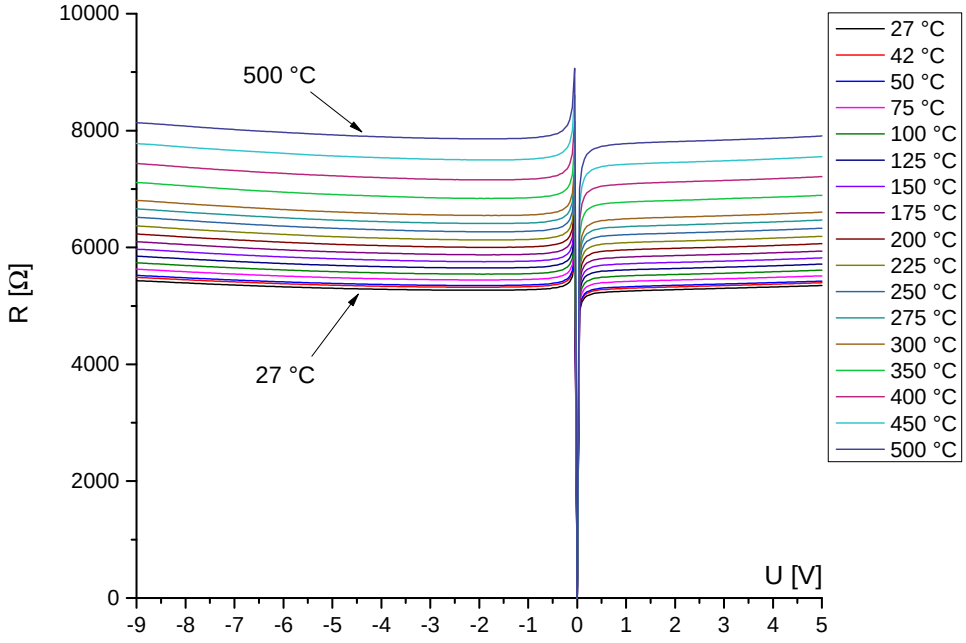

Figure 4.2.: Monitoring change of resistance due to voltage change for different temperatures from 27 °C to 500 °C.

The slope of the lines decreases and the resistance (Figure 4.2) increases at higher temperatures, because of the higher scattering rate of electrons by phonons.
Due to the detector principle of the doped polysilicon wire, which corresponds to a bolometer, it is essential to investigate the resistance change depending on rise of average device temperature. Measurement data evaluation for all four chips between room temperature and 200 °C is shown in Figure 4.3. Higher temperatures are not relevant for our sensing system and were only investigated for completeness in the first step. As one can see from the table in the chart, the proportionality between the change of temperature and the change of resistance, given by the slope values of all chips and obtained by linear fitting through the measurement points, is quite consistent and give an average value of about 0.075 %/°C (in % of average resistance at around 27 °C, which is 5310.82 Ω).

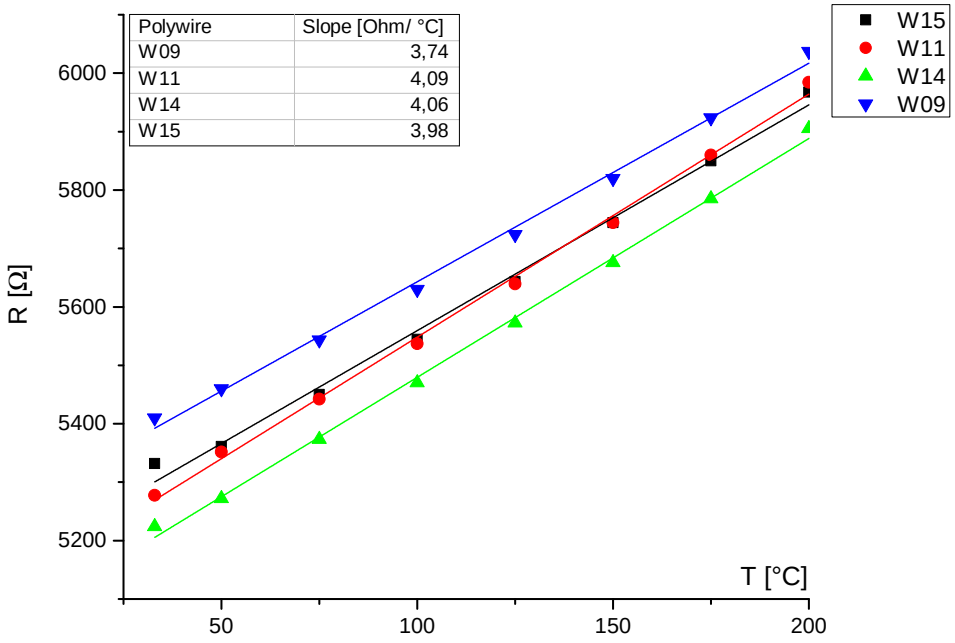

Figure 4.3.: Comparison of resistance change as a function of temperature of four different chips, measured with source meter unit. Eight points respectively are the mean values of measurement data (biased with voltages from 1 to 3 V), lines are the linear fit through the points.

Next step was about investigating the responsivity of the structure.

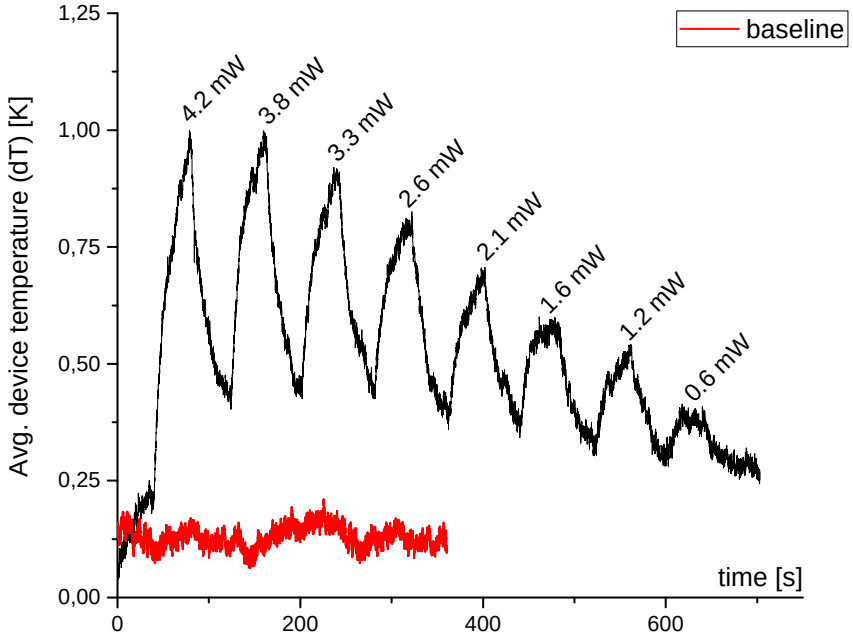

Figure 4.4.: Measurement of average device temperature over time by decreasing the laser power.

The setup used for this experiment is shown in section 3.6.4 Figure 3.13. The laser was tuned to 2400 wavenumbers (4.17 µm), corresponding to maximum laser power and the laser current, which is basically defining the laser power, was set to the maximum. A control measurement with the thermopile powermeter resulted in a maximum laser power of 53 mW at the fiber output for this configuration and alignment. Due to losses caused by incoupling, outcoupling and the waveguide, an average of 8 % of the radiation arrives at the detector, i.e. 4.24 mW. The doped polysilicon wire was biased with a fixed voltage of 5 V by a sourcemeter and the change of resistance was measured simultaneously. Figure 4.4 shows how the detected signal changes as a function of the decreasing laser power. The initial increase of temperature at the beginning of the measurement is due to the voltage applied by the sourcemeter. Then the shutter of the laser output was opened and one can see how the structure is heated up about 0.8 °C at 4.2 mW laser power. Further, the shutter was closed again, laser power set to lower level and after waiting some time for the detector cooling out, opened again. This was done until the signal was smaller than the noise and therefore not detectable. According to the quite slow rising edge and even slower falling edge, it was essential to monitor the heating and cooling behaviour of the structure within the next step of investigation.

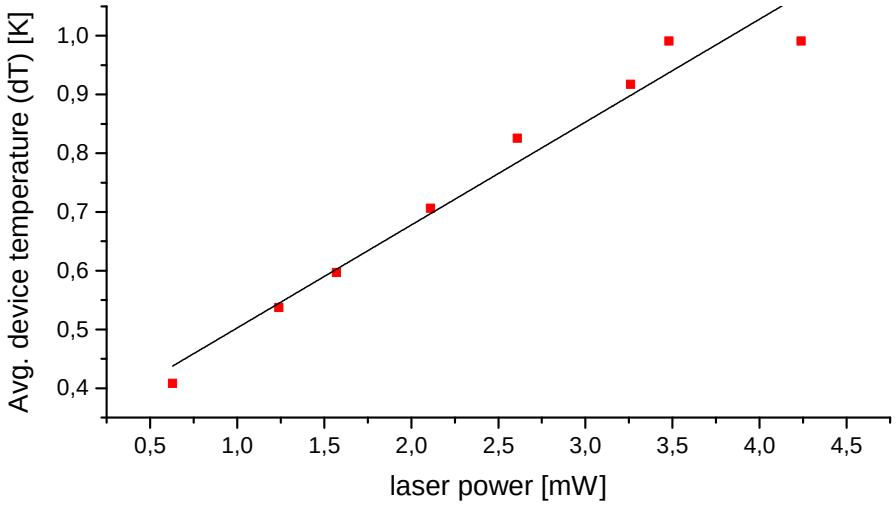

Figure 4.5.: Signal amplitudes in dependence of laser power for detemination of responsivity.

In order to determine the responsivity, the signal amplitudes were plotted as a function of laser power, shown in figure 4.5. The slope of the linear fit through the measurement points gives a responsivity of 0.18 °C/ mW.
To determine the sensitivity, the smallest measurable signal, and the noise equivalent power (explained in section 2.3), a simple baseline was recorded (red line in figure 4.4). For this purpose, the noise of the detector was recorded over a period of about 350 seconds without laser irradiation. The standard deviation of the baseline signal was 0.1 Ω, corresponding to 0.024 °C, resulting in a noise equivalent power (NEP) of $9.32 \cdot 10^{-5}$ W/Hz$^{0.5}$. Accordingly, signals down to around 0.47 mW are measurable, with the current bandwidth of 25 Hz.

In Figure 4.6 the heating and cooling process as an effect of laser irradiation are analyzed in more detail. Sector (a) shows the slight warming up due to the bias field. After the signal stays constant, except of noise, the shutter of the QCL was opened (b). First, there is an abrupt but small increase in the signal due to the actual detector response to mid-IR radiation which takes usually around three measurement steps (average 0.122 s). The further, slow signal increase comes from the heating of the surrounding chip surface. This takes around 70 seconds, until the signal reaches its maximum and stabilizes again. After closing the shutter and therefore stopping laser irradiation, the same effect is visible: first, the signal drops off within a few measurement steps, to a value that corresponds on average to 80 % of the whole signal, followed by a slow signal drop due to the cooling of the

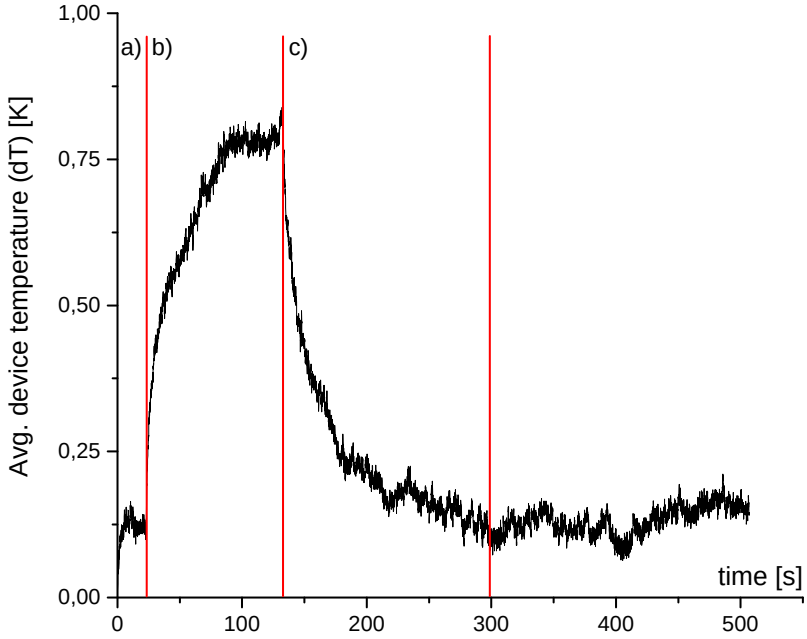

Figure 4.6.: Monitoring of heating/ cooling behaviour of poly wire detector.

surrounding material (c), lasting about 170 seconds until the signal gets back in its initial state. To be suitable as a detector for a CO_2 sensor, the response to direct illumination is too small compared to the response to small temperature changes of the surrounding chip. Furthermore, it can be seen, that the noise is unacceptable high, as it amounts 22 percent of the maximum signal.
To check up the functionality of the etched cavity below the detector structure for thermal isolation, the same measurements were performed on a chip, where the reactive ion etching step was not performed. The resulting structure does not have the cavity below the detector neither the honeycomb pattern below the waveguide (Figure 4.7). The results show that the average responsivity for the polywire detector without cavity, is about 4.5 times lower than for the thermally insulated one.

Due to quite bad responsivity values and much too long heating and cooling time, the polywire was excluded as potential candidate for mid infrared detection and we went on with investigation of other structures.

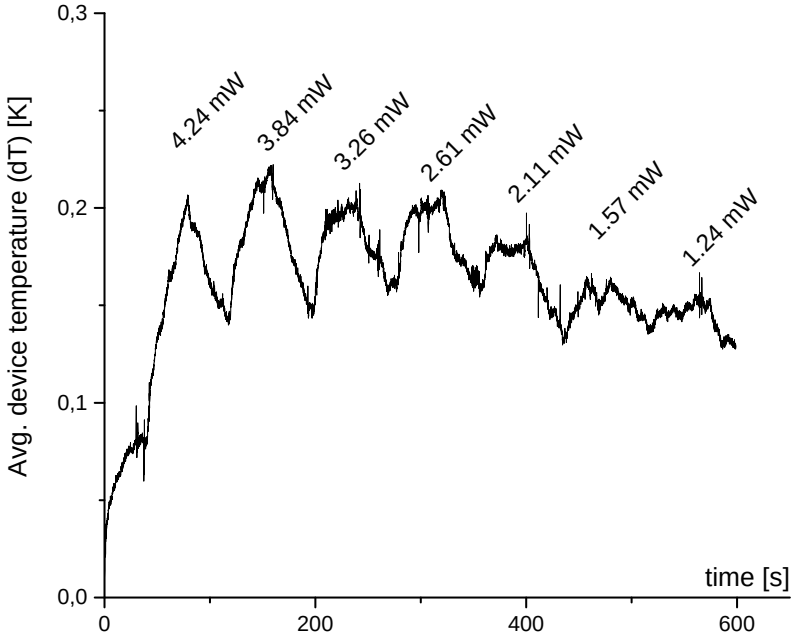

Figure 4.7.: Measurement of average device temperature by decreasing laser power for doped polysilicon wire without etched cavity below detector honeycomb pattern below the waveguide.

4.2. Diode

To be able to investigate responsivity characteristics as a change of average device temperature, like it has been done for the doped polysilicon wire detector above, chips with the diode structures have been mounted into the heating chamber as described in section 3.6.3. Calibration measurements by monitoring current flow biasing with voltages from -9V up to 5V, for temperatures within 25 and 200 °C, gave a set of characteristic curves (Figure 4.8). For higher temperatures the characteristic curves drift to lower forward voltages. This happens because of decreasing internal resistance due to generation of a higher intrinsic carrier concentration, explained in section 2.2.2.

In Figure 4.9 a sensitivity comparison of diode structures on four different chips is shown. The structures were forward biased at 1 V. The dependence of the current as a function of the temperature was modelled linearly. As one can see, three of four devices exhibit almost the same slope from room temperature to 200 °C (relevant linear sector), with an average standard deviation around 1.4% from the mean value, which is $1.515 \cdot 10^{-7}$ A/°C. The diode on chip W11 is not only 22% less sensitive, but also has a five times higher

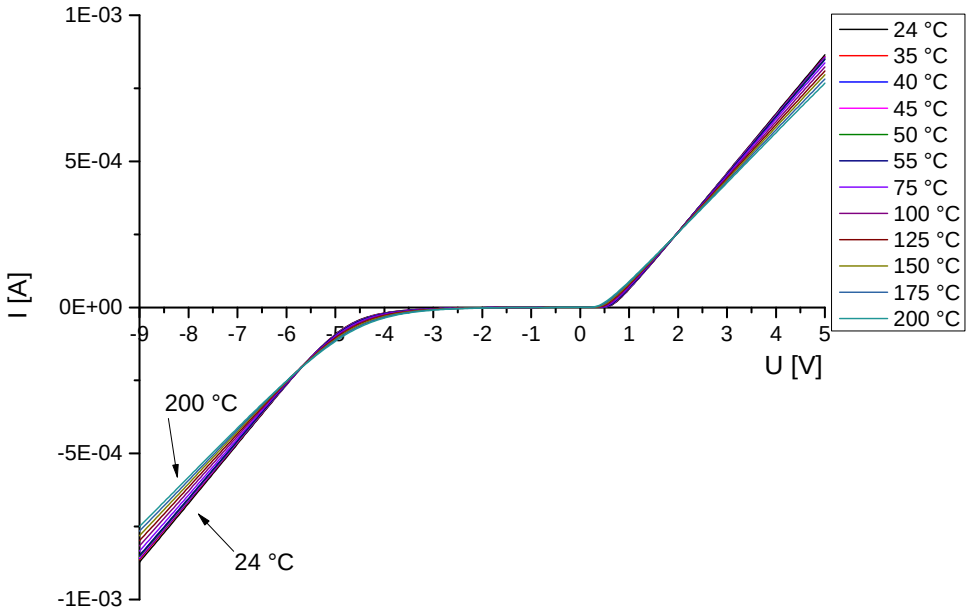

Figure 4.8.: Characteristic curves of a diode for temperatures from 24 to 200 °C.

internal resistance, what can be probably traced back to fabrication tolerances or even defects.

Measurements for responsivity characterization were performed analogous to the polysilicon wire. Current changes upon irradiation at different laser powers were monitored at a fixed bias voltage of 1 V for radiation with 4.17 µm light. In a second step the measured values have been converted back to change of average device temperature, to be able to set up a direct comparison of different detectors. The results are shown in Figure 4.10 and 4.11. The responsivity of the diode is 0.36 °C/mW. When irradiated, first the diode exhibits an abrupt jump, due to thermal heating of the detector structure (Section 2.1.3), followed by slower rising edge, due to warming up of the surrounding substrate. So we took a closer look to of how heating up of the surrounding substrate is influencing the signal. For that the laser beam was focused on the grating at 4.17 µm and 131.5 mW power (Figure 4.12). After opening the shutter, the signal rises abruptly and keeps rising slower (b), for about 15% of the total signal, when stabilized. That means that, considering the total signal, which corresponds to the temperature change between the stabilized baseline and the stabilized heated state, about 15% come from the warming up of the surrounding substrate. The steep ascent in the middle of sector (b) is caused by a mode jump of the

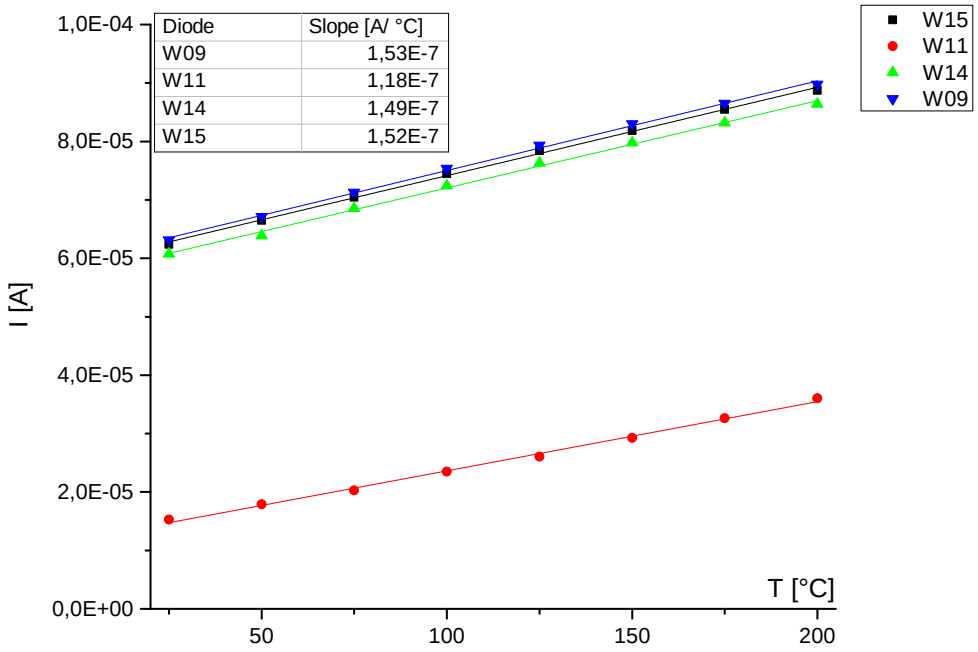

Figure 4.9.: Comparison of current change as a function of temperature of four different chips, measured with source meter at 1 V forward bias voltage. Points are the measured values, lines are the linear fits through the points.

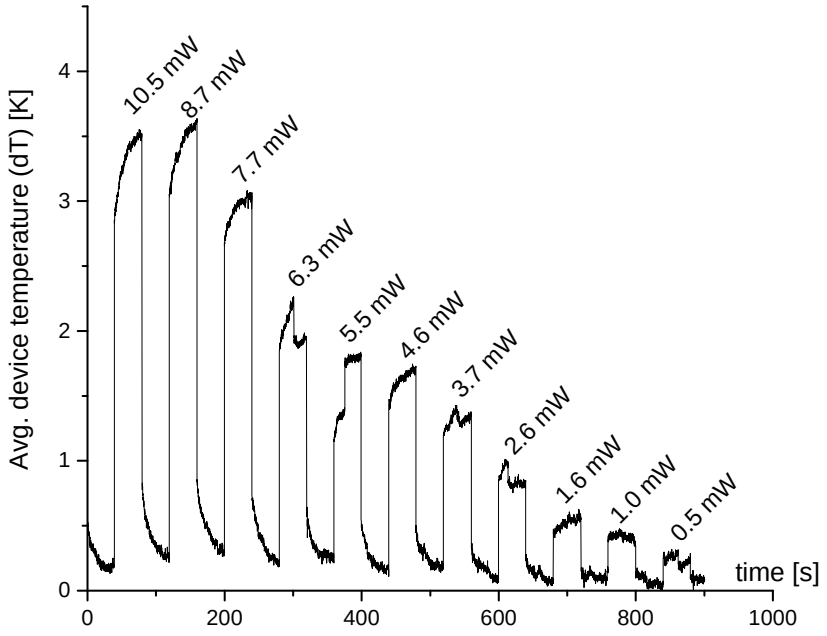

Figure 4.10.: Average device temperature as a function of decreasing laser power, measured over time.

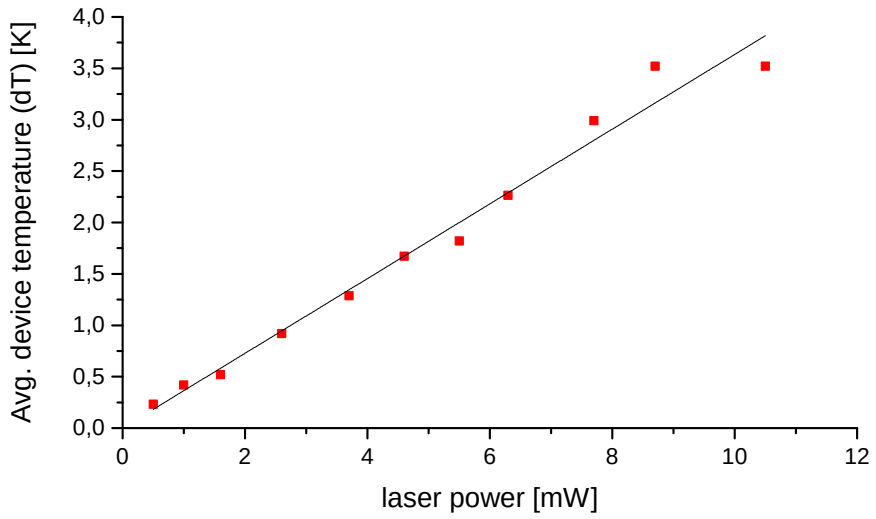

Figure 4.11.: Signal amplitudes in dependence of laser power. Slope of the linear fit gives the average responsivity for the diode detector.

laser. Then the fiber was moved outside the grating, such that the beam illuminates the bare substrate close to the grating (c). By this step the direct thermal effect on the diode detector is interrupted and only the effect due to the heating process of the substrate is measured, which amounts almost 20% of the total signal. After closing the shutter, one can observe the cooling of the substrate material as a decrease of the rest of the signal (d).
So the response of the diode to irradiation is the step we measured when turning on the light (open the shutter), while the slow slope corresponds to the increase of temperature of the substrate. Therefore, the response time of the diode to irradiation is shorter than 40 ms, which is the time resolution of the source meter.

Measurements on diode structures without the etched cavity below the detector for thermal isolation show more than five times lower signals (Figure 4.13).

For determination of the sensitivity and the NEP, a baseline without laser irradiation was recorded and the standard deviation of the noise calculated. Calculations, described in section 2.3, gave a NEP of $1.179 \cdot 10^{-5}$ W/Hz$^{0.5}$ and a measurement capability down to signals of 0.18 mW, what makes it, along with the very fast response, much more interesting for use as detector structure, compared to the doped polysilicon wire.
So we investigated the diode more precisely by measurements with a lock-in amplifier to improve the signal-to-noise ratio and suppress unwanted drifts. For that we biased the diode with a 1.5 V battery and inserted a 15 kΩ resistance between, to reduce the applied voltage and therefore stay compareable with the source meter measurements. Then a set of

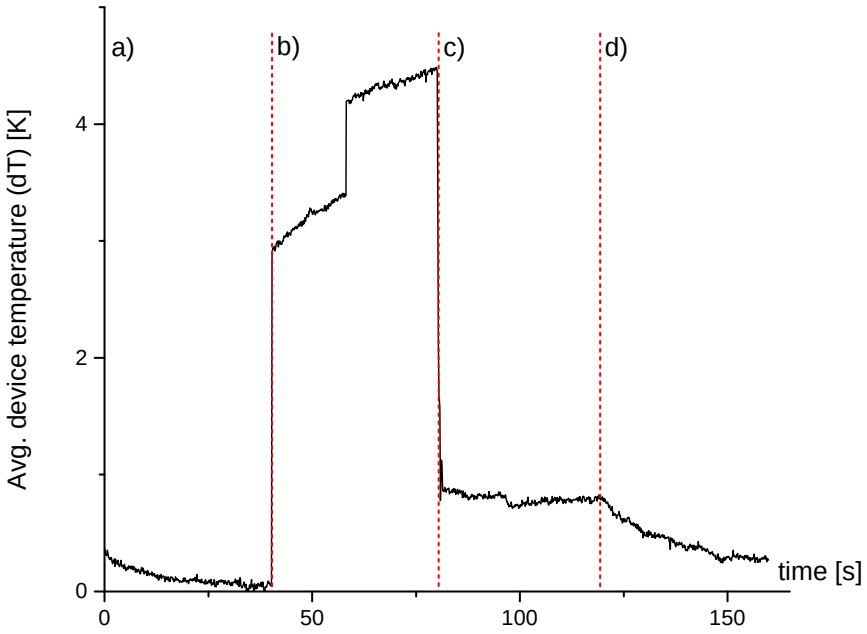

Figure 4.12.: Monitoring signal component, affected by warming up the substrate.

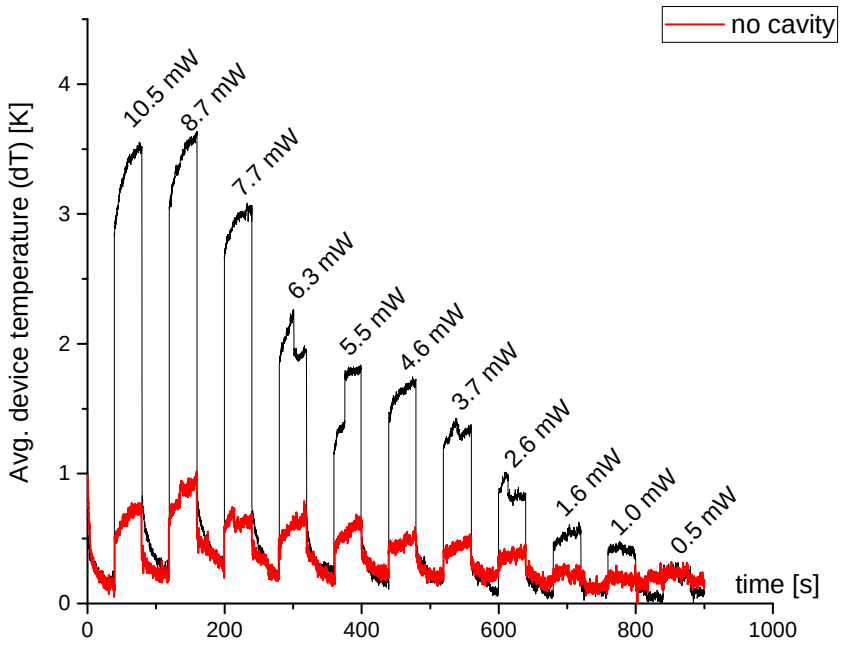

Figure 4.13.: Comparison of diode response to laser irradiation with and without etched cavity below the detector structure. Thermal isolation on average enhances response by factor 5.

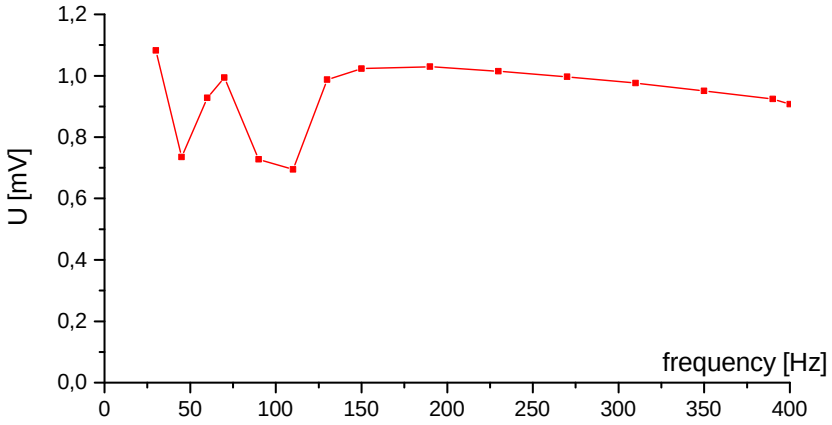

Figure 4.14.: Frequency dependent measurements with lock-in amplifier.

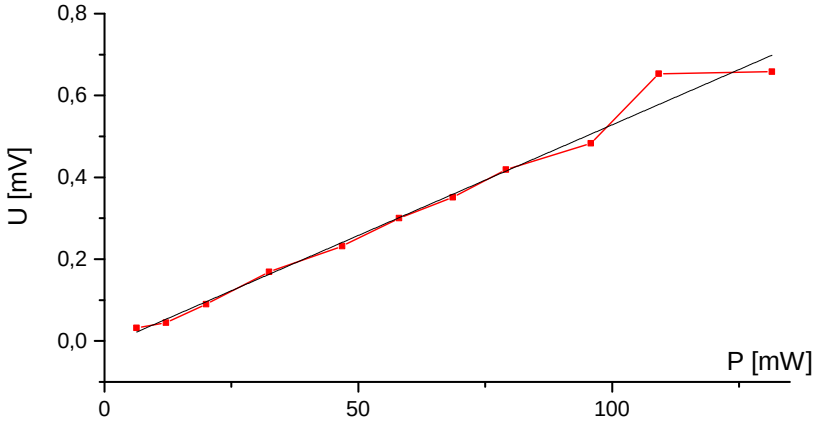

Figure 4.15.: Detected signal as a function of laserpower (squares) and its linear fit (solid line) according to a function $U = a + b \cdot P$ with $a = -0.0124$ and $b = 0.067$.

different measurements has been done.

First a chopper was mounted between the laser output and the fibre incoupling system. The laser was operated in continuous wave mode at 950 mA laser current. Tuned to 4.17 µm wavelength and 10.5 mW laserpower, the beam was irradiated onto the diode, while the chopper frequency got changed from 30 to 400 Hz (4.14). Values for 50 Hz and 100 Hz in figure 4.14 are probably perturbed by frequency filters of the lock-in. Apart from them, the signal stays quite stable until 225 Hz, which corresponds to a response time of 4.4 ms, and then starts to decrease slightly. This verifies an excellent response behavior of the diode.

Power dependent measurements performed at 70 Hz are shown in Figure 4.15 and, similar to what observed for the measurements with the sourcemeter, give a linear proportionality for the signal as a function of the laser power (Figure 4.15). Figure 4.16 depicts again

the signal behavior, when the fibre is moved to the side of the grating, by turning the micrometer screws of the stage. The beam therefore impinges on the substrate close to the waveguide and we can check the influence of the heated substrate on the detector signal. Compared to previous measurements with the source meter, using the lock-in detection we now got rid of the signal drift caused by a heating of the substrate.

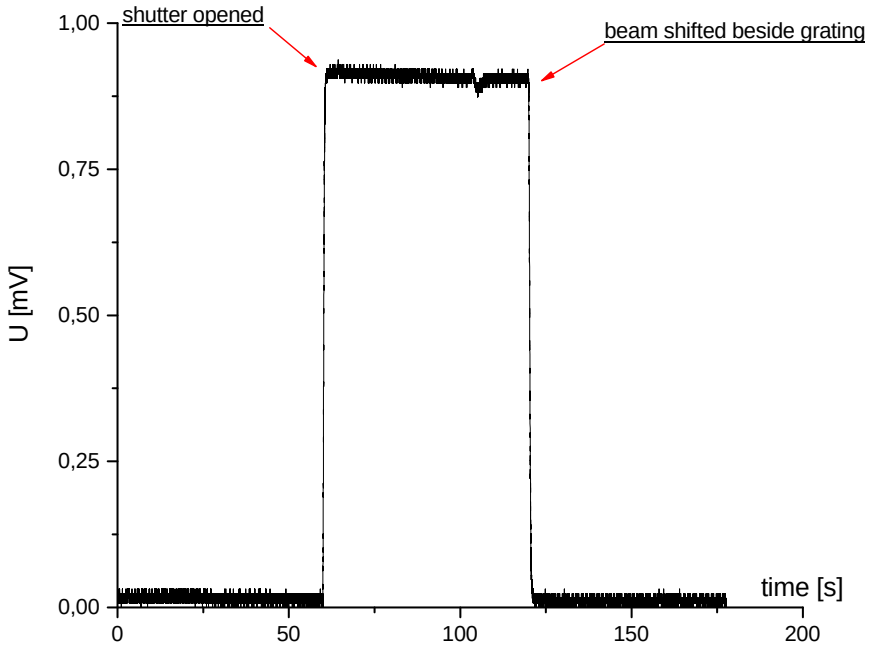

Figure 4.16.: Diode signal by 10.5 mW laser power irradiation and signal behavior after moving the beam from the grating (analogous to Figure 4.12).

4.3. VERD

Finally, we came to the characterization of the vertical cavity enhanced detector.
The VERD structure has been fabricated in four different shapes: two of them circular (C6-5 and C5-5), two rectangular (R3-5 and R4-5), differing in the size of silver surface of the heater (Figure 4.17). Using the total surface size and the surface of meander turns, the Ag coverage has been determined for all structures (Table 4.1). The Ag coverage is defined as the total surface of the detector minus the substrate loops between the Ag meanders.

For the VERD, calibration measurements within the heating chamber have been previously performed by Thomas Söllradl and the results, which are reported in table 4.1, were used for the following analysis.

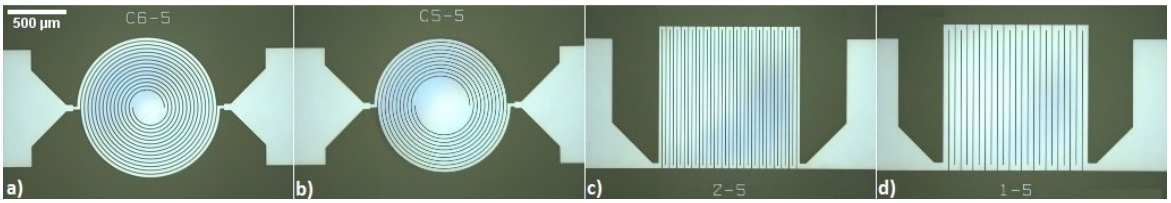

Figure 4.17.: Different silver meander structures, shaping the VERD base. a) C6-5; b) C5-5; c) structure 1-5, which is identical to R3-5; d) structure 2-5, which is identical to R4-5.

Table 4.1.: Data for size of silver meander structures and the temperature coefficient of resistance (analogous to resistivity values for poly wire and diode) for four different shapes of the VERD.

Structure	**Size of Ag coverage** $[mm^2]$	**Temp. coefficient** $[m\Omega/\mathbf{K}]$
C6-5	1.100775	97.54
C5-5	1.010603	77.37
R4-5	1.244100	118.90
R3-5	1.258300	51.92

For investigation of the spectral absorption profile of the structures, absorption measurements with an FTIR microscope had been done for the VERD detectors. The photonic crystal structures should be tailored for 4.26 µm, which is quite accurate the center of the CO_2 absorption band, FTIR measurements show an absorption maximum of around 4.12 µm, as shown in Figure 4.18.

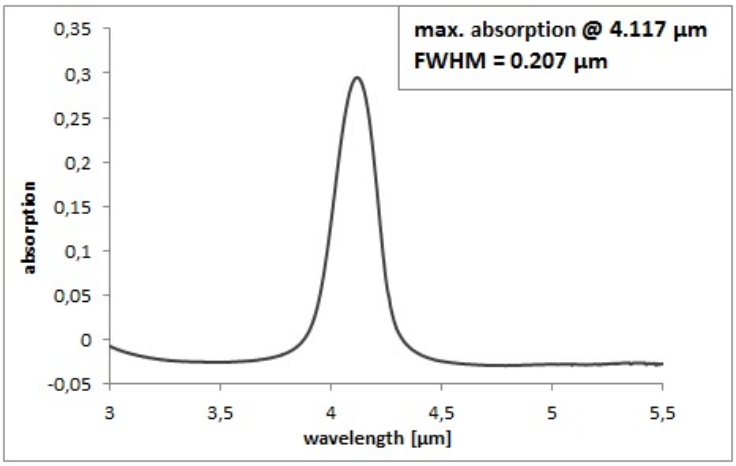

Figure 4.18.: Absorption spectrum of a VERD structure, measured by LUMOS FTIR microscope.

This shift to lower wavelengths might come to some extent from fabrication tolerances, which induce deviations in the layer thicknesses, but in largest part it comes from the angular distribution of the incident light. Indeed, as seen in Section 2.2.3 the VERD absorption has a strong dependence from the angle of the incident light (Figure 2.14). The angular distribution is due to the Cassegrain focusing optics of the FTIR microscope (see Section 3.6.2 and Figure 3.10). The focusing mirror of the Cassegrain objective, which has a numerical aperture of 0.6, corresponding to an aperture angle of approximately 36.8 degrees, is not in parallel to the sample holder, but tilted at a certain angle. Although the exact parameters of the focusing optics are not known, we found the parameters for a typical 8 times objective in literature [55], which gave us 23.2 degrees for the divergence angle β and a working distance of $(\sqrt{5}+2)\cdot f$ for the second mirror which reflects the light onto the sample, where f is the working distance of a Schwarzsschield type objective. So we expect that the incident light is coming from angles between 13.6 and 36.8 degrees. For checking up, whether this is actually the reason for relocation of the wavelength values, we modelled the shift induced by the Cassegrain objective using Matlab (Appendix A). The script takes as an input the wavelength-dependence of the VERD structure, which was simulated by G. Pühringer (JKU Linz). After specifying the fixed values for aperture angle and divergence angle, as stated above, wavelengths for these angles are extracted from the simulation data. Based on the given focal length of the LUMOS FTIR microscope, which is 3 cm, the working distance of the second mirror is calculated. With the working distance of the entire objective infinitesimal annular areas are calculated in increments of 0.2 degrees (corresponding to the increments of the simulation data), which represent the

cross section of the light beam. The central ring has the highest intensity, which decreases with increasing radius according to a Gaussian profile. This means that outer rings, which are formed by shorter wavelengths, have lower intensities, but at the same time larger surfaces. To fit the measured absorption data, the full width at half maximum (FWHM) of the gaussian function was manually changed. So we found a FWHM of $\sigma/2.8$, where σ is the standard deviation. In the end the script plots the absorbed intensities as a function of the wavelengths. The resulting absorption spectrum now had to be multiplied by a scaling factor to match the amplitude. The numeric data is then saved in a textfile. So it is possible to converge and fit the simulation with the measurement data, shown in figure 4.19.

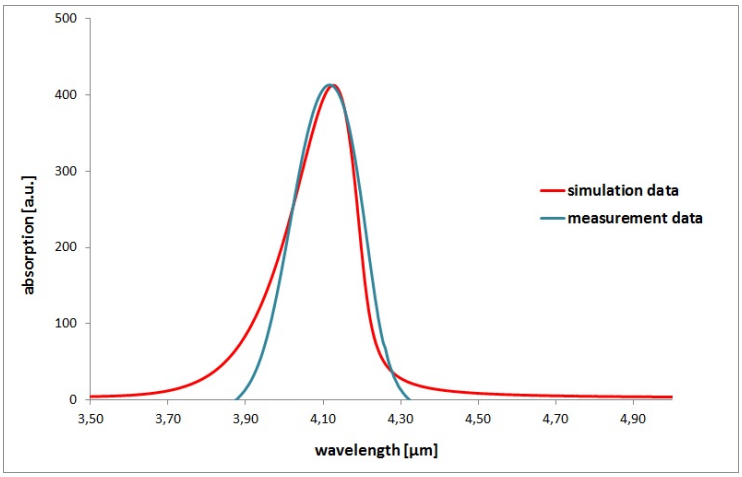

Figure 4.19.: Comparison of FTIR microscopy measurement data and absorption simulation data, tilted for a minimum angle of 13.6 degrees and a divergence angle of 23.2 degrees.

Further deviation might come from fabrication tolerances and or differences in the light distribution at the sample with respect to the simple model used in the script.
Next step was to take analogous absorption measurements by use of the laser setup. Therefore, the beam was again coupled into a fibre and coupled out in front of an optical system composed of two identical plano-convex lenses (Section 3.6.4). The first lens collimates the divergent laser beam, the second lens focuses it onto the VERD.
The signal is, like for the polysilicon wire, about the change of ohmic resistance, induced by laser irradiation. With the calibration measurements (Table 4.1) the change of the detector temperature was obtained from the measured resistivity values and again responsivity results will be presented as a change of average device temperature.
The laser current was set to 950 mA operating in continuous wave mode and the emission

wavelength was varied from 3.95 µm to 4.35 µm. This was repeated on three different chips, for all shapes, to improve the statistics. Figure 4.20 shows the mean values for the average device temperature as a function of the wavelength, compared to the previous measured FTIR microscopy data.

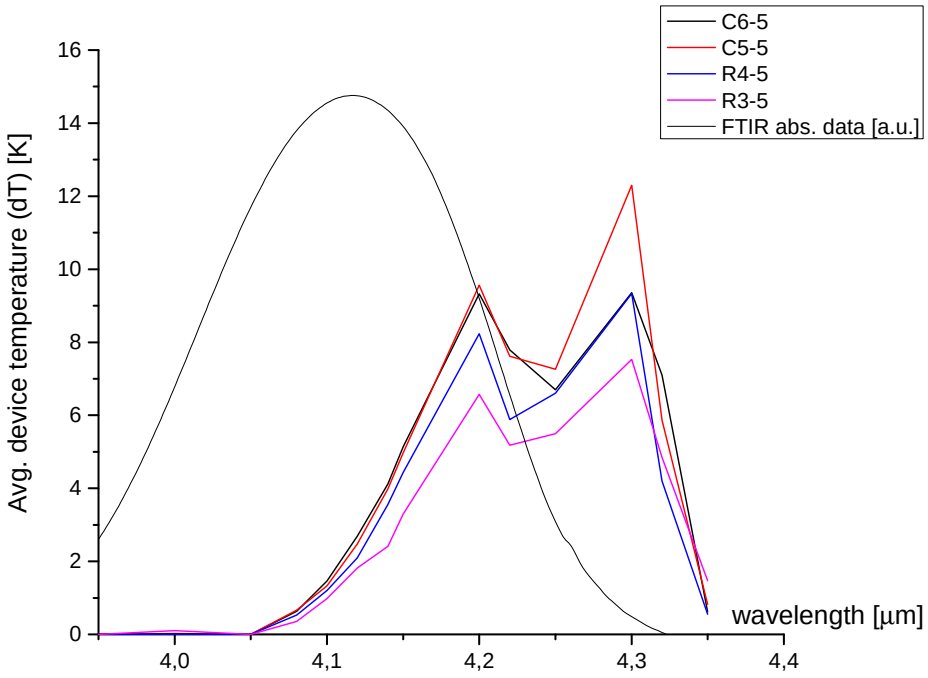

Figure 4.20.: Mean values of average device temperature as a function of the wavelength, obtained from measuring on three different chips, compared to absorption data of structure C6-5, measured by FTIR microscopy (in arbitrary units).

All of the four different shaped structures show the same trend, while the circular ones are performing best. The maximum is shifted to higher wavelength values, compared to the FTIR absorption spectrum. The shape of the measured spectra show a minimum, which is probably due to CO_2 absorption. To better investigate this point, the measurements were repeated with a higher resolution especially within the area of the CO_2 absorption peak. Figure 4.21 shows the results for higher resolution, where it is quite clearly visible that the minimum at 4.23 µm and the maximum at 4.26 µm occur at the maximum and minimum of the CO_2 absorption, respectively. This is not surprising, given the relatively long pathlength in air from the laser to the detector. The same spectral dependence is observed in the recorded laser power at the detector position (Figure 3.14).
The final absorption spectrum of the VERD structures was obtained by dividing the

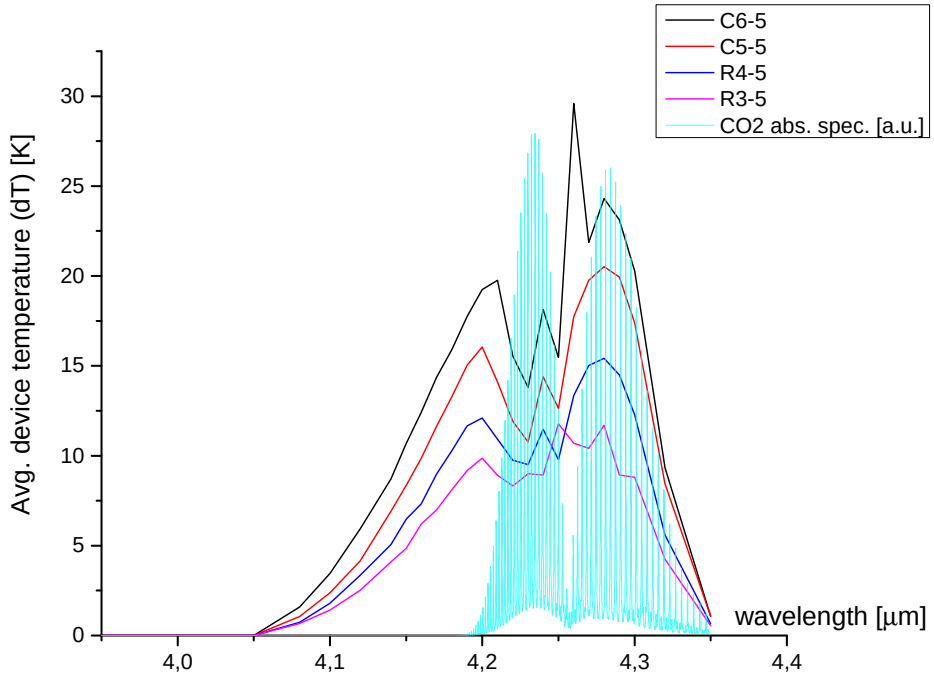

Figure 4.21.: Average device temperature as a function of the wavelength, measured on best performing chip, compared to CO_2 absorption spectrum (in arbitrary units).

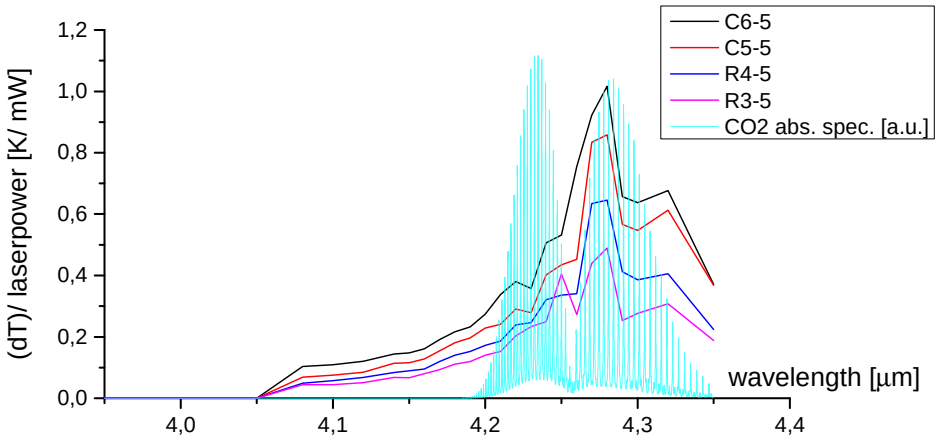

Figure 4.22.: Normalized data: Average device temperature per mW laserpower as a function of the wavelength, compared to CO_2 absorption spectrum (in arbitrary units).

measured signal by the laser power. This provides the amount of temperature change per mW of irradiated power. The result is plotted in figure 4.22. Maximum signal is achieved at 4.27 µm.

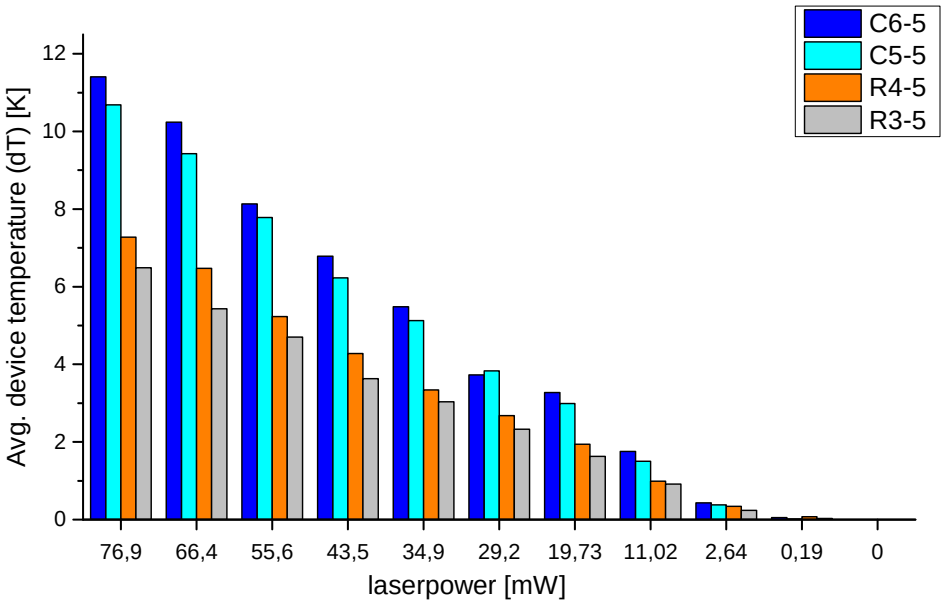

Figure 4.23.: Comparison of signal response of the different VERD structures in dependence of decreasing laserpower.

Subsequently the laser was tuned to 4.17 µm, to avoid effects from the surrounding carbon dioxide and exploit the maximum of laserpower. Then the beam was focused on the four different structures, while increasing the laser current from 730 mA to 950 mA, corresponding to a power increase from 0.19 mW to 76.9 mW. In Figure 4.23 average values for detector temperatures in dependence of the irradiated laser power are shown. It is visible, that best performance was achieved by structure C6-5, followed by C5-5, as already suggested by the measurements shown in Figure 4.21. For measurements at 4.26 µm a much larger response could be reached using the same power and in absence of CO_2 (Figure 4.22). However, in the current setup one has to consider the lower laser power and the absorption from CO_2 in air, whose fluctuations could influence the results and their reproducibility.

Validation of best performance for the circular vertical cavity enhanced detectors led to the interest in finding the reason for that. Table 4.1 assigns larger silver coverage to the rectangular VERDs, what would be a logical contradiction to the operating principle (see section 2.2.3). If we now consider, that in the focus of the lens system, the beam doesn't illuminate the entire detector surface, but has a diameter of around 450 µm (Figure 4.24), this results in new values for the size of the effective detection area, listed in Table 4.2.

Now the difference of the effective detection surface size is only very small. However, it must also be taken into account that in the center, the silver coverage of the circular

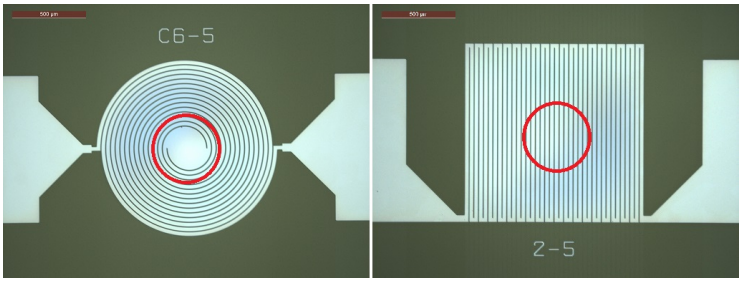

Figure 4.24.: Schematic of the effective illuminated detection area, with a beam diameter of 450 µm. On the left structure C5-6, on the right structure R4-5.

Table 4.2.: Size of effective detection area in dependence of a 450 µm beam diameter.

Structure	**Effective detection surface** $[\mu m^2]$
C6-5	154110
C5-5	159043
R4-5	149615
R3-5	153450

structures has an area in the size range of the light beam cross section, where the entire silicon substrate was etched away. This area is thermally better isolated and, together with the larger effective detection surface, is likely the cause of the better performance, compared to the rectangular structures.
In the next step, we examined the heating and cooling time of the individual detectors, i.e., the reaction time to laser irradiation. It should be considered that even the VERD detector first has an abrupt signal jump when irradiated. Further the signal increases slightly, due to the warming up of the surrounding substrate. The same happens after stopping the irradiation, first the direct detector signal is gone immediately, but the remaining cooling of the material is slow. Therefore, heating and cooling time are defined as the time required for the direct signal response of the detector (Figure 4.25). By closer examination of the individual measurement data, it can be seen that heating and cooling processes usually take one measuring step, approximately 40 ms. According to the best performance of C6-5, this structure has now undergone further investigations.
Again the device temperature was measured as a function of changing laser power at a wavelength of 4.17 µm. This time not only through the multilayer stack of the VERD, but also for the bare silver layer (Figure 4.27).

The strong noise within the signal periods in figure 4.26, best seen at 29.2 mW laser power, can, on this scale, not be intrinsic noise of the detector. Otherwise, these jumps

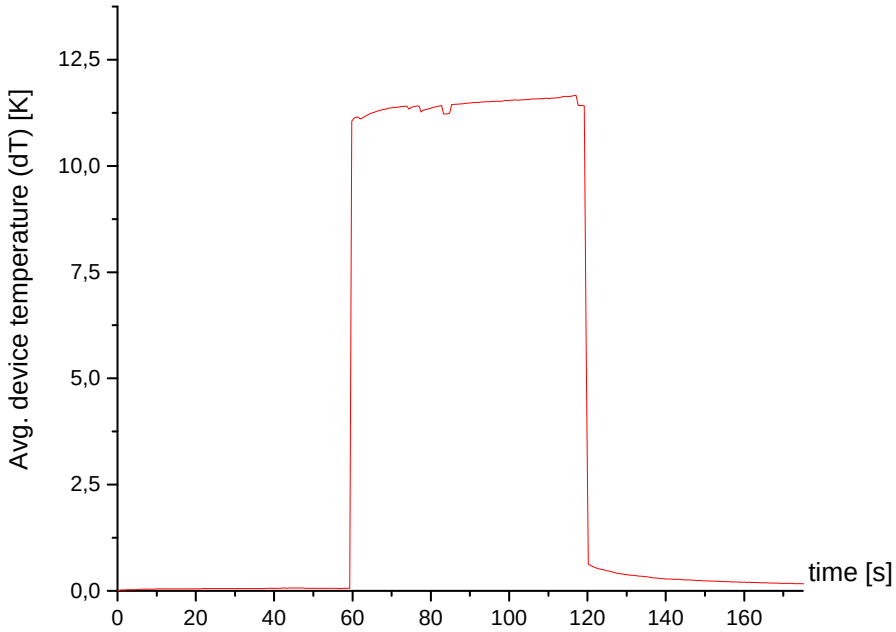

Figure 4.25.: Signal path of C6-5 for irradiation at 76.9 mW laser power. In contrast to the other two detector concepts, the VERD is less dependent on the heating of the surrounding substrate, but still shows an influence of this.

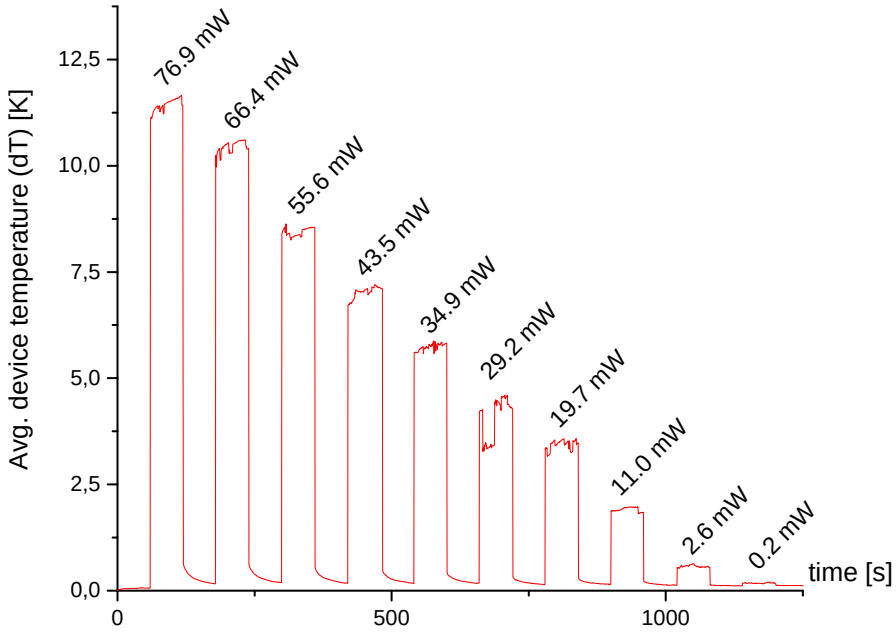

Figure 4.26.: Average device temperature as a function of decreasing laserpower, measured through VERD structure (C6-5).

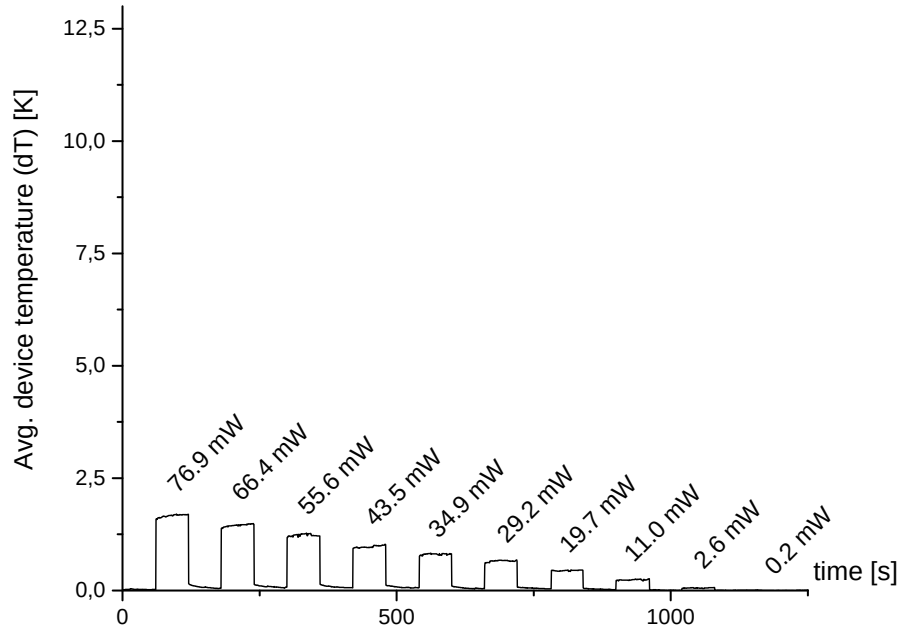

Figure 4.27.: Average device temperature as a function of decreasing laserpower for bare silver illumination (C6-5).

should also appear in the baselines. This suggests that the measurement setup is responsible and caused us to control its stability more closely. To determine the reason for the artifacts, we influenced a measurement in several ways (Figure 4.28). After opening the shutter, we applied manual vibrations to the optical bench, the fibers and the Hirschmann clamps, which connect the detector to the source meter. By far the biggest influence on the signal is caused by movement of the clamps. Therefore, these falsified measurement values were omitted for further calculations of mean values.

Figure 4.29 shows a direct graphical comparison of the signal curves during irradiation of the silver layer and trough the VERD structure. Both curves were fitted by a line and give responsivity values of 0.15 °C/mW for the VERD and 0.021 °C/mW for the bare silver with an average deviation from the best fit of 6.4% and 4.4% respectively. One has to consider, that responsivity for a wavelenth of 4.26 µm is of a factor 4.1 higher (see figure 4.22), i.e. around 0.4 °C/mW. The larger response through the multilayer stack gives an average enhancement of responsivity of a factor 7.1 by VERD, compared to direct silver illumination. For sensitivity determination we again recorded a baseline and calculations give measurement capability down to signals of 0.1 mW and a NEP of $1.738 \cdot 10^{-5}$ W/Hz$^{0.5}$

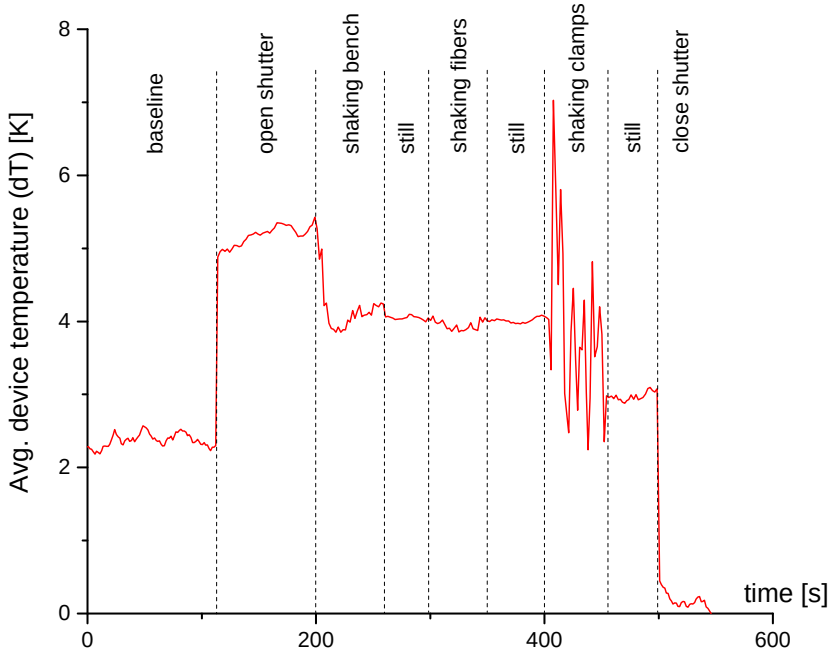

Figure 4.28.: Check up of setup stability my manual influence of a measurement (C6-5).

is achieved. The obtained values make the vertical cavity enhanced detector a favorite for integration into the gas sensing system.

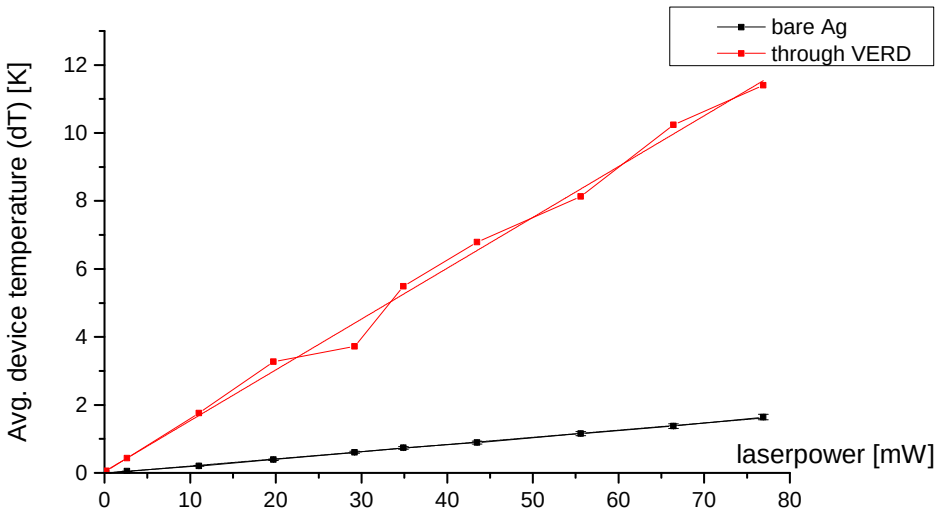

Figure 4.29.: Comparison of response through VERD structure and direct silver illumination (C6-5).

4.4. Discussion and comparison

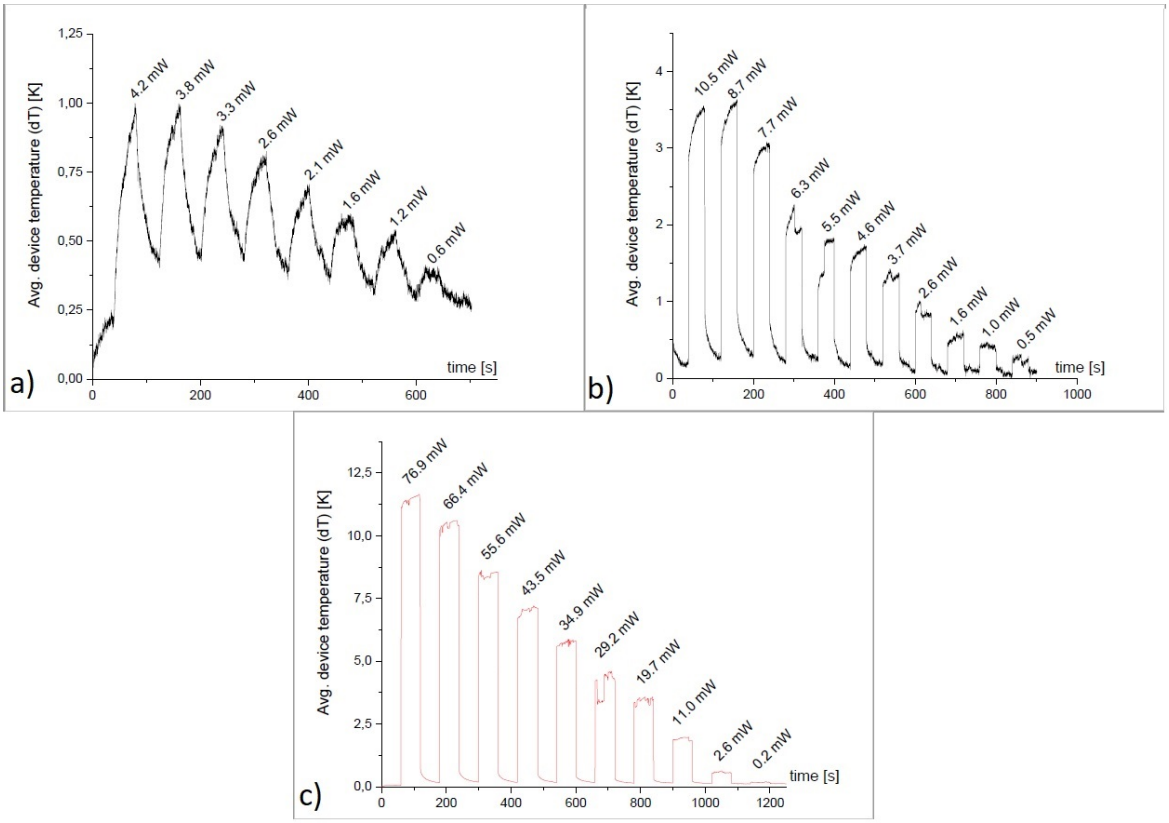

Figure 4.30.: Responsivity for a) polysilicon wire, b) diode, c) VERD.

Table 4.3 summarizes the main results of the detector characterization. The polysilicon wire, the simplest among the three structures, was the first to be investigated. Although the simple construction and fabrication is an advantage of this detector, it would also be necessary to integrate a wavelength selective filter into the sensor system in order to obtain narrowband detection. Measurement results show a relatively small detector response to direct light irradiation compared to the other two structures, while the detector response is dominated by the changes in temperature of the substrate. These findings led us exclude the doped polysilicon wire as a detector for our CO_2 sensor.

The diode, which has a similar fabrication as the polywire, is therefore also a simple, cost-effective detector. Again, however, a wavelength filter would be necessary. Results of the experiments show a 2 times higher responsivity for the diode compared to the polysilicon wire. After 40 ms, which corresponds to the maximum time resolution of the source meter, 80 percent of the maximum signal is present. The remaining 20 percent comes

from warming up the surrounding substrate and has to be considered as an unwanted drift in the measurements. Such an effect can be eliminated by moduling the light source and using a lock-in. With the lock-in even shorter response time could be achieved. All these factors make the diode a potential detector candidate for mid-IR radiation.
Finally, four types of a vertical cavity enhanced detector were characterized. The round structure C6-5 showed the highest responsivity (estimated at a wavelength of 4.26 µm), while also the other three clearly outperformed the polysilicon wire and the diode. Similar to the diode, the response time is limited by the resolution of the source meter and is therefore under 40 ms. The integrated wavelength filter forming the VERD structure, enables narrowband detection. Together with the good results, this makes the VERD the favorite detector for our carbon dioxide sensor.

Table 4.3.: Summary of average results for the three investigated detectors.

	Polysilicon wire	**Diode**	**VERD**
responsivity [°C/ mW]	0.18	0.36	0.40
response time [s]	0.122	0.0044	< 0.04
sensitivity [mW]	0.47	0.18	0.1
NEP [W/ $Hz^{0.5}$]	$9.32 \cdot 10^{-5}$	$1.179 \cdot 10^{-5}$	$1.738 \cdot 10^{-5}$

Conclusion and Outlook

This master thesis focuses on the characterization of three different detector structures for detection of mid-IR light. We investigated a simple doped polysilicon wire (bolometer), a P-N diode and a vertical cavity enhanced detector, in short VERD. All three work on the concept of a thermal detector. Experiments were performed to determine and compare sensitivity, responsivity and response time of the different detectors. For this purpose, the respective detectors were illuminated with a tunable quantum cascade laser at different powers and the response signal was read out via a source meter or lock-in detection. Evaluation of the measurement results and subsequent comparison revealed that the VERD structure performs best, followed by the diode and the polysilicon wire. The VERD detector also offers the advantage of an integrated frequency filter in the form of a Fabry-Perot cavity, which allows narrow-band detection. Compared to the bare silver layer on the backside of the VERD, we achieved a responsivity enhancement of a factor 7.1 through the cavity at a wavelength of 4.17 µm. At 4.26 µm, the peak of the VERD response, we estimate a responsivity enhancement of a factor 28.35 compared to the Ag absorption.
Following future work is planned: First, further detector concepts, including a pyroelectric detector, should be investigated and compared with those, which have been already discussed. In addition, the collaborating teams want to work on the optimization of the VERD structure. Different approaches can be made, mainly regarding the geometry of the silver heater. For example, one could decrease the thermal mass by reducing the thickness of the silver layer and thus enhance the responsivity of the detector.
Finally, the fully integrated sensing system should be realized by combination of the respective components, consisting of emitter, waveguide, detector and frequency filter, if one is needed. Among the challenges is to develop processes to integrate the VERTE (or VERD) with the waveguide structure, as well as to design and produce optimized coupling structures to maximize the light coupling between the vertical-cavity structure and the waveguide.

Appendix A.

Appendix

A.1. Matlab script

```
close all
clear all
% import simulation data
load('wl.mat')
load('theta.mat')
load('matrixTE.mat')
load('matrixTM.mat')
load('spotradianceangle.mat')
load('spotintensityprofile.mat')

matrixTE=MatrixTE';
matrixTM=matrix_TM';
Angle1_deg=0:0.2:37; % absorption simulation data available for 0-37 degrees
% of incident radiation
Angle1=Angle1_deg.*pi/180;


WorkDist=3;  % working distance in LUMOS in cm
f=WorkDist/sqrt(5); % working distance --> for Schwarzschield type,
% it is sqrt(5)f, while the distance "dist" from the second mirror
% is (sqrt(5)+2)f -->
dist=f*(sqrt(5)+2);

% put values here:
MaxAngle=36.8; % aperture angle
MinAngle=13.6; % divergence angle
divangle=MaxAngle-MinAngle;

dA=((2*pi*f^2.*tan(Angle1)./(cos(Angle1)).^2))/2;
dA=dA'; % infinitesimal circular area

cone=MinAngle:0.2:MaxAngle;
conerad=cone.*pi/180;
maxcone=max(cone);
mincone=min(cone);

ind_30deg=search1D(Angle1_deg, (maxcone-mincone));

MaxLambda=max(matrixTE,[],2);
MaxLambdaTM=max(matrixTM,[],2);


for i=1:1:size(MaxLambda)
    wl_ind_max_lambda(i)=search1D(matrixTE(i,:),MaxLambda(i));
    Wl_maxTE(i)=wl(1, wl_ind_max_lambda(i));
```

Figure A.1.

```
    wl_ind_max_lambdaTM(i)=search1D(matrixTM(i,:),MaxLambdaTM(i));
    Wl_maxTM(i)=wl(1, wl_ind_max_lambda(i));
    Wl_max(i)=(MaxLambda(i).*Wl_maxTE(i)+MaxLambdaTM(i).*Wl_maxTM(i))./(MaxLambda(i)+MaxLambdaTM(i));
end

% assumption of Gaussian intensity profile of radiation
sigma=dist*tan(divangle*pi/180)./2.8;
Gaussian_intensity=exp(-(dist*tan(conerad)).^2./(2*sigma^2))./1;
TotI=trapz(conerad, Gaussian_intensity);
Gaussian_intensity=Gaussian_intensity';

for i=(1+mincone*5):1:(1+maxcone*5)
    PartSpectrum(i,:)=dA(i-mincone*5).*matrixTE(i,:);
    PartSpectrum2(i,:)=dA(i-mincone*5).*matrixTE(i,:);
    PartSpectrumGauss(i-mincone*5,:)=(Gaussian_intensity(i-mincone*5,1)'.*dA(i-mincone*5,1))'.*matrixTE(i,:);

end

TotSpectrumLUMOSflat=sum(PartSpectrum)
TotSpectrumLUMOS=sum(PartSpectrumGauss(1:ind_30deg,:),1);
TotSpectrumLUMOStest=sum(matrixTE(1:ind_30deg,:));

figure
hold on
plot(wl, matrixTE(1,:).*500, '-k')
plot(wl, TotSpectrumLUMOS.*10000, '-r')

save('SpectrumLumos.txt', 'wl', 'TotSpectrumLUMOS', '-double','-ascii','-tabs')
```

Figure A.2.

A.2. List of abbrevations

MEMS	Microelectromechanical systems
CMOS	Complementary metal oxide semiconductor
MOX	Metal oxide semiconductor
NDIR	Non-dispersive infrared
IR	Infrared
FWHM	Full width at half maximum
LED	Light emitting diode
QCL	Quantum cascade laser
QW	Quantum well
VERTE	Vertical-cavity enhanced resonant thermal emitter
WG	Waveguide
VERD	Vertical-cavity enhanced resonant thermal detector
PC	Photonic crystal
Q factor	Resonant cavity quality factor
NEP	Noise equivalent power
LP-	Low pressure
PE-	Plasma enhanced
CVD	Chemical vapor deposition
PVD	Physical vapor deposition
MBE	Molecular beam epitaxy
RIE	Reactive ion etching
PCB	Printed circuit board
TC	Thermocompression
TS	Thermosonic
US	Ultrasonic
SEM	Scanning electron microscope
FIB	Focused ion beam
SMU	Source meter unit
LI	Lock-in (amplifier)
CW	Continous wave
FTIR	Fourier-transform infrared
NA	Numerical aperture

A.3. List of symbols

$I(t)$	Output light intensity
$I_0(t)$	Input light intensity
α_λ	Absorption coefficient
λ	Wavelength
λ_0	Vacuum wavelength
ϵ	Emission coefficient
L	Optical path length
C	Concentration of gas sample
Δ	Delta (difference)
ΔE	Energy difference
h	Planck's constant
ν_{vib}	Vibration frequency
v	Vibrational quantum number
J	Rotational quantum number
P	Power
σ	Stefan-Boltzmann constant
A	Surface area
T	Temperature
ΔT	Temperature difference
E	Electric field
a, b	Thermoelectric matter constants
α	Temperature coefficient
R	Resistance
V	Voltage
n	Refractive index
k	Extinction coefficient
c	Vacuum speed of light
ε	Permittivity
ω	Angular frequency
k_{z}	Z-component of the wave vector

Im	Imaginary part of complex value
Re	Real part of complex value
$\boldsymbol{n}$	Complex refractive index
d	Thickness, distance
R	Reflectivity
$\alpha, \beta, \phi, \theta$	Angle
f_{r}	Resonant frequency
σ	Standard deviation
B	Bandwidth
t_{avg}	Average integration time
Y	Yield
j	Current flow
δ	Pathlength
n, m	Integers
ν	Frequency
$S(\nu)$	Lightspectrum
f	Focal length

Bibliography

[1] George F. Fine, Leon M. Cavanagh, Ayo Afonja, and Russell Binions. Metal oxide semi-conductor gas sensors in environmental monitoring. *Sensors*, 10(6):5469–5502, jun 2010.

[2] Jens-Michael Liepe. *Entwicklung und Characterisierung von Halbleitergassensoren zur Online-Detektion der Aromaentwicklung bei Backprozessen.* PhD thesis, Technische Universität München, 2004.

[3] Peter Baumann. *Sensorschaltungen.* Vieweg und Teubner, 2010.

[4] Jane Hodgkinson and Ralph P. Tatam. Optical gas sensing: a review. *Measurement Science and Technology*, 2013.

[5] Sari Lakkis, Rafic Younes, Yasser Alayli, and Mohamad Sawan. Review of recent trends in gas sensing technologies and their miniaturization potential. *Sensor Review*, 34(1):24–35, jan 2014.

[6] Christian Merten and Jan Willmann. Physikalische grundlagen der spektroskopie. 2004.

[7] Christopher Berger. *Photoakustische Spektroskopie zur Emissionsüberwachung.* PhD thesis, Technical University of Munich, 2017.

[8] Kirk H. Michaelian. *Photoacoustic Infrared Spectroscopy.* Wiley, 2003.

[9] Simona M. Cristescu Frans J.M. Harren, Julien Mandon. Photoacoustic spectroscopy in trace gas monitoring. *Encyclopedia of Analytical Chemistry*, 2012.

[10] A Miklós and P Hess. Modulated and pulsed photoacoustics in trace gas analysis. *Analytical chemistry*, 72:30A–37A, January 2000.

[11] J. Kasberger. Spectral resolution of the grating coupler of a miniaturized evanescent field ir absorption sensor. *IEEE Journal of Quantum Electronics 47(7)*, 2011.

[12] M. Schossig, T. Ott, S. Hüller, V. Norkus, and G. Gerlach. 3.4 - efficient thermal infrared emitter with high radiant power. 2015.

[13] G. S. Ranganath. Black-body radiation. *Resonance*, 13(2):115–133, feb 2008.

[14] Patrick Schnabel. *Elektronik-Fibel: Elektronik, Bauelemente, Schaltungstechnik, Digitaltechnik*. Norderstedt : Books on Demand, 2007.

[15] Mattias Borg, Heinz Schmid, Johannes Gooth, Marta D. Rossell, Davide Cutaia, Moritz Knoedler, Nicolas Bologna, Stephan Wirths, Kirsten E. Moselund, and Heike Riel. High-mobility GaSb nanostructures cointegrated with InAs on si. *ACS Nano*, 11(3):2554–2560, feb 2017.

[16] Hiroyuki Yoshinaga, Jun ichi Hashimoto, Hiroki Mori, Yukihiro Tsuji, Makoto Murata, Mitsuru Ekawa, and Tsukuru Katsuyama. Mid-infrared quantum cascade laser integrated with distributed bragg reflector. In Manijeh Razeghi, editor, *Quantum Sensing and Nano Electronics and Photonics XIII*. SPIE, feb 2016.

[17] Christian Mann. *Entwurf und Charakterisierung von Quantenkaskadenlasern*. PhD thesis, Albert-Ludwigs-University Freiburg/ Breisgau, 2004.

[18] Christina Consani Gerald Pühringer Surabhi Lodha Bernhard Jakoby Thomas Grille Thomas Söllradl, Christian Ranacher. Characterization of a resonant-cavity enhanced thermal emitter for the mid-infrared. 2017.

[19] Ivan Celanovic, David Perreault, and John Kassakian. Resonant-cavity enhanced thermal emission. *Physical Review B*, 72(7), aug 2005.

[20] M. A. Butt, S. A. Degtyarev, S. N. Khonina, and N. L. Kazanskiy. An evanescent field absorption gas sensor at mid-ir 3.39um wavelength. *Journal of Modern Optics*, 64(18):1892–1897, may 2017.

[21] Yuewang Huang, Salih K. Kalyoncu, Qiancheng Zhao, Rasul Torun, and Ozdal Boyraz. Silicon-on-sapphire waveguides design for mid-IR evanescent field absorption gas sensors. *Optics Communications*, 313:186–194, feb 2014.

[22] Jost Müller. *Characterisierung integriert-optischer Silizium-Wellenleiter*. PhD thesis, Technical University of Hamburg-Harburg, 2013.

[23] Christian Ranacher, Cristina Consani, Ursula Hedenig, Thomas Grille, Ventsislav Lavchiev, and Bernhard Jakoby. A photonic silicon waveguide gas sensor using evanescent-wave absorption. In *2016 IEEE SENSORS*. IEEE, oct 2016.

[24] Wolfgang Schenk, Friedrich Kremer, Gunter Beddies, Thomas Franke, Petrik Galvosas, and Peter Rieger. *Physikalisches Praktikum*. Springer Fachmedien Wiesbaden, 2014.

[25] Pasqualina Maria Sarro. *Integrated Silicon Thermopile Infrared Detectors*. PhD thesis, Technical University of Delft, 1987.

[26] Hamamatsu. Thermal detectors.

[27] Sidney B. Lang. Pyroelectricity: From ancient curiosity to modern imaging tool. *Physics Today*, 58(8):31–36, aug 2005.

[28] Brian Elias. Recent developments in photoconductive infrared arrays. *SENSOR and TEST Conference*, 2009.

[29] H. Suche. Optoelektronische detektoren. University of Paderborn, 2003.

[30] Hamamatsu. Handbook of si-photodiodes.

[31] Christian Ranacher Surabhi Lodha Thomas Grille Gerald Pühringer Bernhard Jakoby, Thomas Söllradl. Characterization of silver microheaters for vertical-cavity enhanced resonant thermal emission. *IEEESensors*, 2017.

[32] Gerald Pühringer and Bernhard Jakoby. Modeling of a highly optimizable vertical-cavity thermal emitter for the mid-infrared. *Procedia Engineering*, 168:1214–1218, 2016.

[33] Lukas Rauter, Cristina Consani, Thomas Söllradl, and Gerald Pühringer et al. Characterization of a vertical-cavity enhanced detector for narrowband detection in the mid-infrared. 2018.

[34] W.M Steen. Principles of optics m. born and e. wolf, 7th (expanded) edition, cambridge university press, cambridge, 1999, 952pp. 37.50/US $59.95, ISBN 0-521-64222-1. *Optics & Laser Technology*, 32(5):385, jul 2000.

[35] Wolfgang Demtröder. *Experimentalphysik 2*. Springer Berlin Heidelberg, 2013.

[36] Parag B. Deotare, Murray W. McCutcheon, Ian W. Frank, Mughees Khan, and Marko Lončar. High quality factor photonic crystal nanobeam cavities. *Applied Physics Letters*, 94(12):121106, mar 2009.

[37] M. Selim Ünlü and Samuel Strite. Resonant cavity enhanced photonic devices. *American Institute of Physics*, 1995.

[38] Benjamin W. Koegel. *Mikromechanisch weit abstimmbare Oberflaechen-emittierende Laserdioden für Sensoranwendungen*. Cuvillier Verlag Goettingen, 2009.

[39] Hamamatsu. Characteristics and use of infrared detectors, 2011.

[40] Ernst Strasser. *Simulation von Topographieprozessen in der Halbleiterfertigung*. PhD thesis, Technische Universitaet Wien, 1994.

[41] Klaus-Peter Müller. *Praktische Oberflächentechnik*. Vieweg und Teubner Verlag, 2003.

[42] Ivanda Mile. Implementation and development of the lpcvd process. 2011.

[43] Ronald Curley, Thomas McCormack, and Matthew Phipps. Low-pressure cvd and plasma-enhanced cvd.

[44] Friedrich-Wilhelm Bach, Andreas Laarmann, and Thomas Wenz, editors. *Modern Surface Technology*. Wiley-VCH Verlag GmbH & Co. KGaA, jul 2006.

[45] Dominik Güttler. Echtzeit-in-situ-messung der oberflächenbelegung einer magnetronkathode bei der reaktiven sputter-abscheidung. Master's thesis, Forschungszentrum Rossendorf, 2004.

[46] René A. Haefer. *Oberflächen- und Dünnschicht-Technologie*. Springer Berlin Heidelberg, 1987.

[47] Friedrich-Wilhelm Bach, Andreas Laarmann, Kai Möhwald, and Thomas Wenz, editors. *Moderne Beschichtungsverfahren*. Wiley-VCH Verlag GmbH & Co. KGaA, nov 2004.

[48] Dietrich Widmann, Hermann Mader, and Hans Friedrich. *Technologie hochintegrierter Schaltungen*. Springer Berlin Heidelberg, 1988.

[49] Avinash P., Logeeswaran V.J., and Saif Islam M. Wet and dry etching. *University of California, Davis*.

[50] Christian Harlander. *Numerische Berechnung von Induktivitäten in dreidimensionalen Verdrahtungsstrukturen*. PhD thesis, Technische Universität Wien, 2002.

[51] Mohamad Sbeiti. *Thermomechanische Beschreibung der Ausbildung einer intermetallischen Phase beim Ultraschall-Wedge/Wedge-Drahtbonden im Rahmen der Theorie der materiellen Kraefte*. PhD thesis, Technische Universtitaet Berlin, 2013.

[52] Eckard Macherauch and Hans-Werner Zoch. *Praktikum in Werkstoffkunde*. VIEWEG und TEUBNER, 2011.

[53] Dr. Christine Kranz and Prof. Boris Mizaikoff. Mikroskopie mit fokussierten ionenstrahlen. *GIT-Labor - Portal für Anwender in Wissenschaft und Industrie*, 2013.

[54] ARCoptix S.A. Basics: Fourier transform spectrometry. Chemin de Trois-Portes 18, 2000 Neuchatel, Switzerland.

[55] Max J. Riedl. *Optical Design Fundamentals for Infrared Systems, Second Edition*. SPIE, mar 2001.

[56] THORLABS. *Reflective Microscope Objectives*.